Evaluating Wettability of Calcareous Shales from the Duvernay Formation: Effect of Petrophysical Properties, Thermal Maturity, and Natural Fractures

by

Shiyu Xu

A thesis submitted in partial fulfillment of the requirements for the degree of

Master of Science

in

Petroleum Engineering

Department of Civil & Environmental Engineering

University of Alberta

ABSTRACT

Recent advances in horizontal drilling and multi-stage hydraulic fracturing technologies have led to rapid development of unconventional oil and gas resources to meet the increasing energy demand. In particular, organic-rich shales are considered important resource plays worldwide. In order to design successful hydraulic fracturing and enhanced oil recovery operations, one should have a detailed understanding of rock properties of these organic-rich shales and their hydrocarbon recovery potentials.

Spontaneous imbibition (SI) tests have been used to evaluate hydrocarbon recovery potential in unconventional reservoirs. In this study, we conducted SI tests on calcareous shale plugs from 5 wells drilled in the Early-oil (EOW) and oil windows (OW) in East Shale Basin (ESB) of the Duvernay Formation. The results were compared with those of siliceous samples from the West Shale Basin (WSB) of Duvernay formation to investigate effects of kerogen maturity on oil and brine uptake. We characterized EOW plugs based on the results of tight-rock analysis (TRA), x-ray diffraction (XRD), and rock-eval pyrolysis. We compared the SI results and petrophysical properties with those of highly-mature and siliceous plugs in the oil and gas windows in the West Shale Basin (WSB) of the Duvernay. We investigated the relationships between SI results and petrophysical properties of ESB plugs to understand the effects of kerogen maturity and rock mineralogy on SI and pore structure of organic-rich shales. We also investigated the effects of organic-pore connectivity and fractures on wettability of the EOW plugs. By using CT scan images, we divided EOW plugs into highly-fractured (HF), slightly-fractured (SF), and non-

fractured (NF) plugs. We used reservoir oil and conducted comparative imbibition tests on selected core plugs to investigate effects of fracture intensity on imbibition profiles.

The ESB plugs are categorized as calcite-rich shale (calcareous shale) that are rich in organic matter (average total organic carbon (TOC) of 5.5 wt%) with significantly high value of Hydrogen Index (HI >600). The results of SI tests show that oil wettability index (WI_o) of ESB plugs is positively correlated with production index (PI) and T_{max}, but not with TOC content. We hypothesize that the low oil imbibition in plugs with high TOC content is due to poor connectivity of their organic pores, and we test this hypothesis by analyzing SEM images and conducting nitrogen sorption tests. The lack of well-developed organic pores within organic matter of the EOW plugs is confirmed with SEM images. The results of nitrogen sorption tests show that micro and fine mesopores (< 10 nm) within organic matter are more abundant in OW plugs than in EOW plugs. The poor connectivity of pores can also be confirmed by observing a large portion of pore space not being accessed by oil when comparing the normalized imbibed volume of oil with the corresponding porosity value. We also observed that the normalized Imbibed volume of oil is much higher in the HF and SF plugs compared with that in the NF plugs. The results suggest that the fractures enhance accessibility of isolated pores, leading to more connected pore network for oil imbibition. This observation suggests that fracture porosity plays a significant role in wetting behavior of the EOW plugs. We also concluded that the porosity measured by Boyle's law helium-porosimetry using crushed EOW samples can be overestimated due to enhanced accessibility of isolated pores. This is because crushing the samples enhances accessibility of isolated pores considered as ineffective porosity under intact conditions. Combined analyses of imbibition

profiles and core images of the fractured plugs show that oil rapidly imbibes into the fracture system, and then gradually imbibes from fractures into rock matrix.

PREFACE

This thesis is an original work by Shiyu Xu.

The tight rock analysis (TRA), X-ray diffraction (XRD), and rock-eval pyrolysis in Chapter 2, (in 2.2.1, 2.2.2, 2.2.3, respectively) and CT scan images in Chapter 5 (in 5.1.1) were conducted by commercial companies.

Chapter 3 and 4 has been published as Xu, S., Yassin, M. R., Dehghanpour, H., & Kolbeck, C. (2022). The Effects of Kerogen Maturity on Pore Structure and Wettability of Organic-rich Calcareous Shales. Journal of Molecular Liquids.

Chapter 5 of this thesis has been published as Xu, S., Yassin, M. R., Dehghanpour, H., & Kolbeck, C. (2020, September). "Wettability of Calcareous Shales from the East Duvernay Basin: The Role of Natural Fractures, Thermal Maturity, and Organic-Pore Connectivity". In SPE Canada Unconventional Resources Conference. OnePetro.

I was responsible for conducting laboratory experiments, analyzing the experimental data as well as writing and editing these papers. Christen Kolbeck was responsible for reviewing the paper and securing company approvals for publishing the paper. Mahmood Reza Yassin was responsible for reviewing the paper and providing technical feedbacks. Hassan Dehghanpour was the supervisory author and was responsible for reviewing the paper and providing technical feedbacks.

DEDICATION

Dedicated to my dearest parents,

Mrs Ling liu, and Mr. Yifei Xu,

and my beloved grandparents.

ACKNOWLEDGEMENTS

I would like to express my gratitude and respect to my supervisor, Dr. Hassan Dehghanpour for his continuous guidance, support, and encouragement throughout my MSc program. Without these help from him, this thesis would not be complete.

I am deeply grateful to my parents Mrs. Ling Liu and Mr. Yifei Xu for their moral and financial support. They are always understanding and supportive whenever I had a difficult time.

I would like to give my special thanks to Dr. Mahmood Reza Yassin for his valuable comments, suggestions, and assistance on my research. I would also like to thank Yue Shi for his contribution in conducting rock/fluid experiments and analyzing SEM images.

I would like to thank my past and present colleagues (Lin Yuan, Mohammad Yousefi, Yanze Zhang, Mohammad Hossein Doranehgard, Maryam Eghbalvala, Yingkun Fu, Mohammad Sabbir Hossain, Son Tran, Tamer Moussa, Amin Alinejad, Jestril Ebaga Ololo, and Taregh Soleiman Asl) for their insightful contributions and valuable discussions.

I would also like to thank Guy Grierson for significant technical discussions and Outlier Resources Ltd. for providing rock and fluid samples as well as petrophysical data. This work was supported by Future Energy Systems Program and Natural Sciences and Engineering Research Council of Canada (NSERC).

Table of Contents

List of Tables

List of Figures

Nomenclature

BV	Bulk volume, L^3 [cm^3]
HI	Hydrogen Index, dimensionless
$(I_o^{eq})_{BV}$	Normalized imbibed volume of oil [% BV]
$(I_o^{eq})_{PV}$	Normalized imbibed volume of oil [% PV]
$(I_w^{eq})_{BV}$	Normalized imbibed volume of brine [% BV]
$(I_w^{eq})_{PV}$	Normalized imbibed volume of brine [% PV]
OI	Oxygen Index, dimensionless
PI	Production Index, dimensionless
PV	Pore volume, L^3 [cm^3]
S_1	Free hydrocarbons constant, M/M [mg/g]
S_2	Hydrocarbons generated from kerogen, M/M [mg/g]
S_3	CO_2 produced during pyrolysis of kerogen, M/M [mg/g]
S_g	Gas saturation, L^3/L^3 [%PV]
S_o	Oil saturation, L^3/L^3 [%PV]

S_w	Water saturation, L^3/L^3 [%PV]
T_{max}	Temperature of maximum hydrocarbon yield [^oC]
TOC	Total Organic Carbon, M/M% [wt%]
WI_o	Oil wettability index, dimensionless

Abbreviations

BJH	Barrett-Joyner-Halenda analysis
CT	Computerized tomography
DFT	Density Function Theory
EDS	Energy-dispersive x-ray spectroscopy
EOW	Early-oil window
ESB	East Shale Basin
FNF	Filled natural fracture
GR	Gamma ray
HF	Highly-fractured
I/M	Illite/Mica
I/S	Illite/Smectite
LPGS	Low-pressure gas sorption
nD	NanoDarcy

NMR	Nuclear magnetic resonance
NF	Non-fractured
OGW	Oil and gas windows
OM	Organic matter
PSDs	Pore size distributions
SEM	Scanning electron microscopy
SF	Slightly-fractured
SI	Spontaneous imbibition
TRA	Tight-rock analysis
WCSB	Western Canadian Sedimentary Basin
WSB	West Shale Basin
XRD	X-ray diffraction

Chapter 1

Introduction

1.1 Background

Recent advances in horizontal drilling and multi-stage hydraulic fracturing technologies have led to rapid development of unconventional oil and gas resources to meet the increasing energy demand. In particular, organic-rich shales are considered important resources worldwide. During hydraulic fracturing, a large volume of fracturing fluid (2 to 4 million gallons per well) is injected into the formation (Council, G. W. P., 2009). Understanding and modeling the mechanisms for fluid transport in formation matrix are essential for designing successful hydraulic-fracturing and enhanced-oil recovery operations.

Characterizing the pore network and evaluating the wettability of shales have been the focus of various recent studies. The compositional complexity, heterogeneity, and low porosity of organic-rich shales can lead to inaccurate wettability evaluation by contact-angle tests. Instead, spontaneous imbibition (Takahashi and Kovscek, 2010; Lan et al., 2015) and nuclear magnetic resonance (NMR) (Odusina et al., 2011; Sulucarnain et al., 2012; Sigal, 2015) are commonly used recently to study wettability of shales in order to understand their pore structure (Gao et al., 2019). Spontaneous imbibition is a capillary-driven process used to study the mechanisms of hydrocarbon potential and recovery in shale reservoirs (Takahashi and Kovscek, 2010; Lan et al., 2015; Kesserwan et al., 2016; Liang et al., 2018). Kesserwan et al. (2016) performed NMR analysis on

highly-laminated carbonated source rocks and studied the effect of clay content and total organic carbon (TOC) content on the shale wettability. Their NMR results showed a mixed-wet shale matrix with preference of oil while brine was flowing along bedding planes that are rich in clay minerals. Liang et al. (2018) tested spontaneous imbibition of 2 wt% KCl solution into a thin section of tight organic-rich carbonate rock to observe morphological and mineralogical changes on the fracture surface before and after being exposed to the imbibing fluid. They found that calcite dissolution increases permeability of the rock sample. Odusina et al. (2011) performed NMR analysis to monitor brine and oil imbibition into carbonate-rich Eagle Ford samples and observed a mixed-wet behavior with a preferentially higher wetting affinity to brine. They concluded that total organic carbon (TOC) content and fractures control oil and brine imbibition, respectively. Overall, understanding pore structure of organic-rich shales can be challenging due to their compositional complexity, heterogeneity, and low porosity.

Low-pressure gas sorption tests (LPGS) have been used to characterize pore structure of shales in previous studies (Adesida et al. 2011; Clarkson et al. 2012; Labani et al. 2013; Zolfaghari et al. 2017). Labani et al. (2013) used low pressure nitrogen adsorption method to characterize pore system of gas shales. Their gas adsorption analysis results show an inverse relationship between pore surface area and pore size, suggesting that micropores with higher surface area are important for gas shale production. They also concluded that increasing TOC content, thermal maturity, and clay content also increases the abundance of micro- and mesopores, increasing the volume of adsorbed gas. Clarkson et al. (2012) conducted low-pressure nitrogen adsorption analysis on intact core plugs to determine the pore size distribution of tight gas siltstone samples. They used two

types of isotherm interpretations which are the Barrett-Joyner-Halenda (BJH) analysis and Density-functional theory (DFT) to determine pore size distributions (PSDs). They found that samples with the lowest TOC and illite content have the largest dominant pore-throat size and highest permeability. Zolfaghari et al. (2017) characterized organic and inorganic pore volume and PSDs of gas shales samples by comparative analysis of nitrogen sorption tests using BET method and modified water sorption experiments. Their results indicate relatively smaller organic pores than inorganic pores.

The dependence of fluid uptake by shales on TOC content and thermal maturity has been studied recently. (Hu et al., 2016; Yassin et al., 2017; Jagadisan and Hedari, 2019; Begum et al, 2019; Yang et al., 2019). Yang et al., (2019) characterized the effect of mineral composition, TOC content, and pore structure on the spontaneous imbibition in Lower Jurassic Dongyuemiao shales by a combined analysis of scanning electronic microscopic images, nitrogen physisorption, and mercury intrusion porosimetry. Their results suggest that the connectivity of both hydrophilic and hydrophobic pore networks is enhanced in shales samples with higher TOC content. Yassin et al. (2017) conducted spontaneous-imbibition tests on Duvernay plugs to study the relationship between organic-shale wettability and petrophysical properties such as TOC content, effective porosity, and thermal-maturity level. They concluded that higher wetting affinity of shales toward oil is attributed to the abundance of well-connected hydrophobic nanopores within the organic matter. Begum et al. (2019) conducted spontaneous-imbibition tests on organic-rich shale plugs from different intervals of the Duvernay Formation to study the effects of kerogen-maturity level on organic-shale wettability. Their results indicate that equilibrated imbibed oil is negatively

correlated with TOC content due to the poorly-connected organic pore network of less-mature Upper Duvernay samples. In addition to previous studies focusing on oil potentials in siliceous shales, oil potential of early-mature shales has not been well studied and there are very few studies investigating the effect of thermal maturity on pore structures of calcareous source rocks.

Natural fractures can contribute to shale permeability (Gale and Holder, 2010), and fracture intensity is considered a controlling factor in shale production (Curtis, 2002; Vega et al., 2014). Multiphase transport through fractured shales has been studied recently (Prodanocic et al., 2010; Chi and Heidari, 2014; Landry et al., 2014; Kesserwan et al., 2016). Landry et al. (2014) conducted an image-based study to investigate the connectivity between matrix and the calcite-filled natural fractures in Eagle Ford shales. Their results show that cemented microfractures are permeable and their permeability is within nano-Darcy range. Kesserwan et al. (2016) performed NMR analysis on highly-laminated source rocks and studied the effects of pore connectivity on fluid transport. They found that both brine and oil can imbibe into the fractures. They concluded that the presence of fractures can enhance the connectivity of both hydrophilic and hydrophobic pores. They also compared the porosity values measured on crushed samples using gas pycnometer and by NMR technique and concluded that using crushed samples can overestimate the effective porosity. Roychaudhuri et al. (2013) studied water imbibition into shale samples from Appalachian Basin and concluded that initial rate and volume of water uptake are controlled by the permeability and volume of the microfracture network of the shale samples. They also concluded that the microfracture permeability is higher than the matrix permeability in orders of magnitude, through observing a significantly slower water imbibition into the sample's matrix than that into the

microfracture network.

WSB of Duvernay Formation has been the focus area in our previous studies on siliceous shales. However, ESB has not been well studied in terms of their oil potentials in relating to their TOC-rich characteristic. The purpose of this study is to evaluate the effects of thermal maturity level and organic-pore connectivity on spontaneous imbibition and pore structure of the organic-rich calcareous shales from Duvernay's ESB (**Figure 1a**). We characterized ESB samples based on their petrophysical properties. We conducted oil and brine SI tests, LPGS, scanning Electron Microscopy (SEM), and Energy-dispersive X-ray Spectroscopy (EDS) analyses. We compared the results with those of siliceous WSB samples (Yassin et al., 2017; Begum et al., 2019) to investigate the effects of mineralogy and thermal-maturity level on pore structure and wettability**.**

1.2 Objectives of Research

The objectives of this study are as follows:

1) Characterizing the wettability of calcareous East Duvernay shales and compare them with the siliceous West Duvernay shales. Investigating the effects of different petrophysical properties on oil wettability index.
2) Investigate the effect of kerogen maturity on organic-pore generation in organic-rich shales and oil uptake by them.
3) Investigating the effects of osmotic pressure and water adsorption on brine imbibition by calcareous shales.
4) Investigate the effect of fractures on oil imbibition by organic-rich shales.

1.3 Thesis Structure

Chapter 1 briefly introduces the research background, research gap, and objectives of this study.

Chapter 2 introduces the Duvernay Formation and describe the porosity, permeability, minerology, TOC, and rock-eval pyrolysis results of East Duvernay core plugs.

Chapter 3 presents the results of oil and brine spontaneous imbibition tests and comparison of petrophysical properties and wettability index between ESB and WSB core plugs.

Chapter 4 presents the results of low-pressure nitrogen gas sorption test and SEM/EDS analysis.

Chapter 5 presents the oil imbibition results on ESB core plugs with different fracture intensity.

Chapter 6 summarizes the main findings and conclusions of this study and provides recommendations for future studies.

Chapter 2

Background and Petrophysical Properties of Duvernay Formation

2.1 Overview and Background of Duvernay Formation

The organic-rich carbonates, shales, and siliceous mudstones of Duvernay Formation in the Western Canadian Sedimentary Basin (WCSB) are source rocks which have become a major target for unconventional oil/gas exploration and development in Canada (Marshall et al., 2019). The total in-place resources are estimated to be 350 to 540 trillion cubic feet of natural gas, 7 to 16 billion barrels of natural gas liquids, and 44 to 81 billion barrels of oil. This formation belongs to the Frasnian age and is part of the Upper Devonian Woodbend group and was deposited in areas where stratigraphically-equivalent Leduc Formation and reefs are present (Stoakes, 1980; Marshall et al., 2019).

The two main areas of the Duvernay Formation are the West Shale Basin (WSB) and the East Shale Basin (ESB), as shown in **Figure 1a**. The Duvernay Formation overlies the carbonates of the Cooking Lake platform in ESB, while it overlies most of Majeau Lake Formation except for Wild River area in WSB as shown in **Figure 1b** (Wendte et al, 1998). WSB is separated into upper and lower shale units by a middle-carbonate layer. The Upper and Lower Duvernay Formations are rich in clay and silica minerals in WSB and they have higher TOC content compared with the middle-carbonate layer (Marshall et al., 2019). ESB is surrounded by the shedding of reef-derived detritus of carbonate materials from the Leduc reefs and platforms. In contrast to WSB, ESB shales

cannot be divided into distinct zones due to the shedding of these carbonate materials from Leduc reefs and depositing within ESB. The ESB shales are rich in carbonate minerals and have a variable TOC content (Switzer et al., 1994; Marshall et al., 2019). **Figure 1a** shows the five studied wells located in the area of interest.

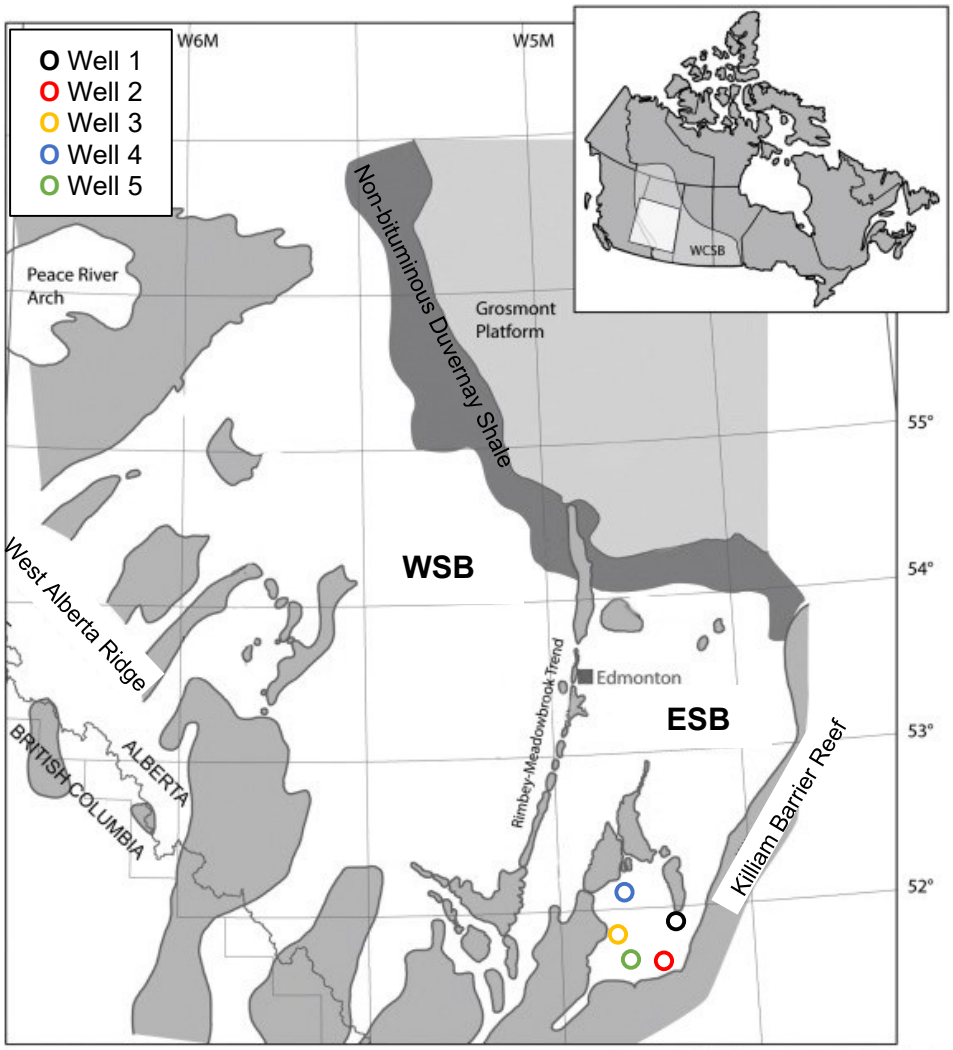

(a)

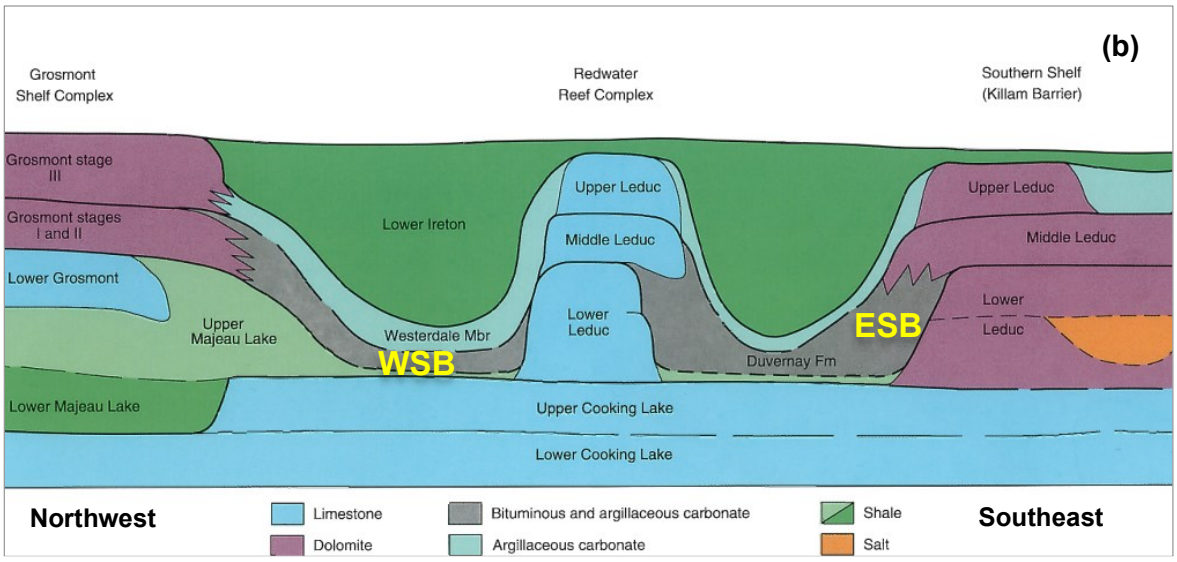

Figure 1 — (a) Location of the Duvernay Formation in Alberta, divided into East Shale Basin (ESB) and West Shale Basin (WSB) (Revised form Wang et al., 2016). The core samples in this study are from the wells in the ESB. (b) Stratigraphic cross section showing the vertical distribution of Duvernay Formation (color grey) (Revised from Switzer et al., 1994).

2.2 Core Plugs from Duvernay Formation

Here, we present the results of tight-rock analysis (TRA), X-ray diffraction (XRD) analysis, and rock-eval pyrolysis of the East Duvernay core plugs used in this study.

2.2.1 Tight-Rock Analysis (TRA)

Table 1 lists bulk density, matrix density, porosity, permeability, and initial fluid saturations of the offset samples close to the candidate core plugs. The core plugs are labeled as $W_{1\text{-}1}$ through $W_{5\text{-}2}$ with the depth ranging from 1970.42 to 2392.20 meter, respectively. Bulk density, grain

density, porosity, fluid saturations, and absolute permeability are also measured on offset samples near our core plugs. Porosity ranging from 0.67% (W_{1-10}) to 10.76% (W_{2-3}) of bulk volume is measured by using Boyle's law porosimetry on crushed samples with 30/35 mesh size cleaned by Dean Stark extraction method (Dean and Stank, 1920) and dried at 110°C. Pressure-decay permeability ranging from 0.2 nD (W_{4-2}) to 177 nD (W_{3-1}) is the absolute gas permeability measured by pressure-decay method on clean and dry crushed samples with 20/35 mesh size.

Table 1 — Tight-rock analysis (TRA) of the Duvernay's ESB samples.

Sample ID	Core Depth (m)	Offset Depth (m)	Bulk Density (g/cm^3)	Grain Density (g/cm^3)	Porosity (%BV)	S_w (%PV)	S_o (%PV)	S_g (%PV)	Permeability (nD)
W_{1-1}	1970.42	1970.00	2.41	2.43	1.56	5.7	34.1	60.2	49
W_{1-2}	1972.06	1970.95	2.47	2.48	1.03	4.4	61.8	33.8	-
W_{1-3}	1973.62	1973.90	2.42	2.43	1.91	4.7	69.8	25.5	60
W_{1-4}	1976.57	1976.35	2.52	2.53	1.24	7.5	52.6	39.9	51
W_{1-5}	1993.65	1993.85	2.29	2.31	2.13	2.0	63.1	35.0	79
W_{1-6}	1996.96	2001.30	2.43	2.45	2.34	7.6	53.5	38.9	80
W_{1-7}	1999.15	2001.30	2.43	2.45	2.34	7.6	53.5	38.9	80
W_{1-8}	2001.70	2002.15	2.62	2.64	1.02	0.0	47.6	52.4	52
W_{1-9}	2004.71	2002.55	2.38	2.40	1.85	0.0	66.4	33.6	63
W_{1-10}	2015.52	2013.65	2.67	2.70	0.67	14.7	44.1	41.3	-
W_{2-1}	2193.58	2193.70	2.54	2.65	4.72	21.0	15.0	64.0	54
W_{2-2}	2216.00	2216.30	2.65	2.72	3.59	72.0	9.0	19.0	17
W_{2-3}	2229.53	2229.70	2.23	2.44	10.76	18.0	28.0	54.0	49
W_{3-1}	2223.90	2224.08	2.43	2.56	6.25	4.7	54.6	40.7	177
W_{3-2}	2231.10	2230.80	2.68	2.72	1.91	52.4	18.7	28.9	2
W_{3-3}	2262.85	2262.87	2.68	2.71	1.04	15.5	25.2	59.3	0.5
W_{4-1}	2314.30	2313.53	2.56	2.62	2.98	10.7	52.8	36.5	25
W_{4-2}	2336.00	2335.48	2.66	2.68	0.75	22.4	25.6	52.1	0.2
W_{4-3}	2344.20	2344.45	2.48	2.52	2.28	20.6	71.2	8.2	16
W_{5-1}	2389.42	2389.50	2.47	2.57	4.49	6.8	46.8	46.4	48
W_{5-2}	2392.20	2392.90	2.54	2.63	3.83	15.7	33.8	50.5	34

2.2.2 Minerology

Table 2 lists the XRD data from the offset samples, representing the mineralogy of the selected core plugs. According to Table 2, calcite is the dominant non-clay mineral and its concentration ranges from 27 wt% to 92 wt%, followed by quartz ranging from 2 wt% to 31 wt%. Illite/mica (I/M) mixed layers are the dominant clay minerals while illite/smectite (I/S) mixed layers and chlorite are negligible in most samples. Core plug $W_{2\text{-}3}$ with 31 wt% of total clay content is the most clay-rich sample. $W_{4\text{-}3}$ has the highest content of quartz (31 wt%) and Ankerte/Fe-dolomite (23 wt%) and the least content of calcite that is only 27 wt%.

Table 2 — Minerology of the ESB Duvernay samples. The unit of XRD results is wt%.

Sample ID	Quartz	K-Feldspar	Calcite	Ankerte/Fe-Dolomite	Dolomite	Pyrite	Barite	Total non-clay	Illite/Smectite (I/S)	Illite/Mica	Kaolinite	Chlorite	Total Clay
$W_{1\text{-}1}$	9	4	65	1	1	2	1	82	4	12	1	1	18
$W_{1\text{-}3}$	11	5	59	1	6	2	0	83	3	13	1	1	17
$W_{1\text{-}4}$	11	7	41	1	16	2	0	78	8	13	0	1	22
$W_{1\text{-}5}$	11	5	72	0	5	2	0	94	0	6	0	0	6
$W_{1\text{-}8}$	13	6	55	1	11	2	0	86	3	11	0	0	14
$W_{2\text{-}1}$	4	5	84	1	-	1	-	94	-	-	-	0	6
$W_{2\text{-}2}$	6	0	85	9	-	0	-	100	-	-	-	0	0
$W_{2\text{-}3}$	10	12	42	7	-	5	-	76	-	-	-	1	24

W_{3-1}	10	1	75	2	-	1	-	89	2	9	-	0	11
W_{3-2}	6	0	80	3	-	1	-	90	2	5	-	3	10
W_{3-3}	5	1	86	0	-	3	-	95	0	5	-	0	5
W_{4-1}	4	1	93	0	-	1	-	99	0	1	-	0	1
W_{4-2}	7	0	89	0	-	1	-	97	0	3	-	0	3
W_{4-3}	31	8	27	23	-	4	-	93	0	6	-	0	7
W_{5-1}	10	2	77	2	-	3	-	94	0	6	-	0	6
W_{5-2}	2	0	92	2	-	1	-	97	0	3	-	0	3

2.2.3 Rock-Eval Pyrolysis

According to Van Krevelen (Van Krevelen, 1950) diagram presented in **Figure 2a**, the kerogen type of samples from Well 1, 2 and, 5 is classified as Type I. However, the Duvernay rocks have a clear evidence of marine environment, consistent with its marine regional setting. Therefore, it is not possible for the ESB kerogens to be deposited in a lacustrine environment and form kerogen Type I. The marine depositional environment of ESB forms kerogen Type II with the potential to produce a mix of oil and gas (Requejo et al. 1992). The unexpected Type I kerogen identified in **Figure 2a** is due to the very low oxygen index (OI) and the very high hydrogen index (HI), indicating extreme reducing conditions, and extremely high level of kerogen preservation, respectively. The extreme reducing conditions was likely developed during restricted-basin conditions with very stagnant water and high algae production. Under such conditions, no grazing organisms are able to survive, leading to not only high kerogen production but also full kerogen preservation.

The crossplot of production index (PI) vs. T_{max} is shown in **Figure 2b**. All samples shown are in the oil zone, while Well 3, 4, and 5 samples have higher level of kerogen conversion compared to samples from well 1 and 2. The maturity level of Well 1 and 2 is in early-oil window with low level of kerogen conversion.

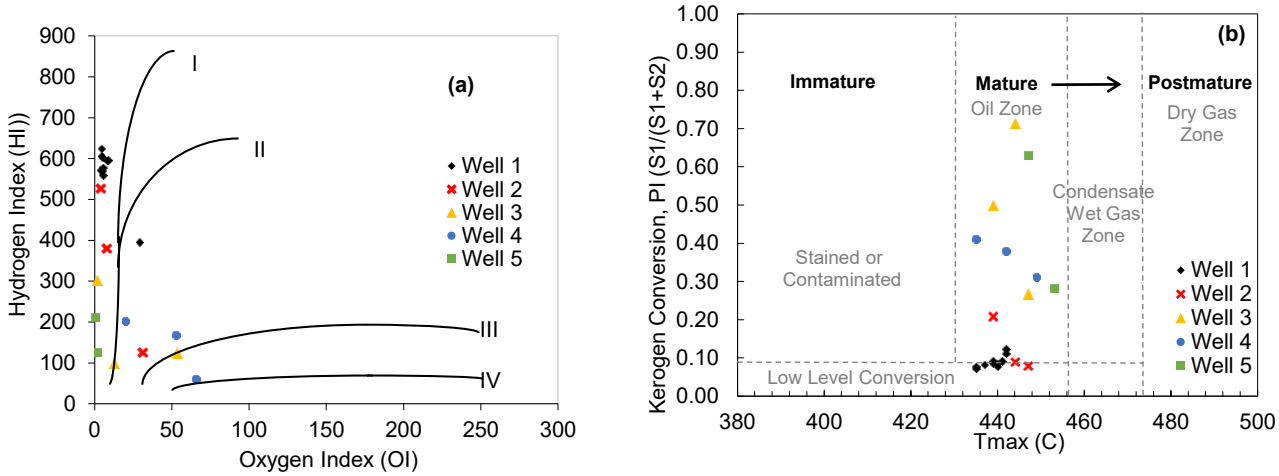

Figure 2 — The crossplots of (a) HI vs. OI for identifying kerogen type, and (b) PI vs. T_{max} for determining kerogen maturity level. The crossplot of PI vs. T_{max} shows that the ESB samples are in the oil zone with varying level of kerogen conversion.

Table 3 lists the results of rock-eval pyrolysis conducted on the offset ESB samples. TOC content ranges from 0.08 wt% (W_{3-3}) to 14.45 wt% (W_{3-2}). Production index (PI) and T_{max}, showing the level of thermal maturity, range from 0.08 (W_{1-1}) to 0.71 (W_{3-2}), and 435°C (W_{1-1}) to 454°C (W_{5-2}), respectively.

Table 3 — Rock-eval pyrolysis results of offset samples from ESB

Sample ID	Core Depth (m)	Offset Depth (m)	TOC (wt%)	S_1 (mg/g)	S_2 (mg/g)	S_3 (mg/g)	T_{max} (°C)	HI	OI	PI
W_{1-1}	1970.40	1970.00	8.00	3.59	45.80	0.31	435	573	3.9	0.07
W_{1-2}	1972.10	1970.95	5.87	2.79	32.88	0.31	435	560	5.3	0.08
W_{1-3}	1973.60	1973.90	9.63	5.27	58.40	0.44	437	606	4.6	0.08
W_{1-4}	1976.60	1976.35	4.98	2.52	29.66	0.39	440	596	7.8	0.08
W_{1-5}	1993.70	1993.85	11.78	6.44	68.10	0.63	439	578	5.3	0.09
W_{1-8}	2001.70	2001.30	7.27	4.46	43.95	0.37	441	605	5.1	0.09
W_{1-9}	2004.70	2002.55	7.16	4.15	44.77	0.33	440	625	4.6	0.09
W_{2-1}	2193.58	2193.70	3.15	1.19	12.03	0.26	444	381	8.0	0.09
W_{2-2}	2216.00	2216.30	0.89	0.30	1.13	0.27	439	126	31.0	0.21
W_{2-3}	2229.53	2229.70	12.67	5.63	66.90	0.49	447	528	4.0	0.08
W_{3-1}	2223.90	2224.08	5.35	3.22	16.17	0.10	447	302	1.9	0.27
W_{3-2}	2231.10	2230.80	0.32	0.40	0.40	0.17	444	125	53.1	0.71
W_{3-3}	2262.85	2262.87	0.08	0.04	0.08	0.01	439	100	12.5	0.50
W_{4-1}	2314.30	2313.53	0.45	0.26	0.72	0.23	444	160	51.0	0.27
W_{4-2}	2336.00	2335.48	0.67	0.49	1.07	0.27	442	160	40.0	0.31
W_{4-3}	2344.20	2344.45	2.35	2.92	4.77	0.47	442	203	20.0	0.38
W_{5-1}	2389.42	2389.50	14.45	6.64	30.72	0.04	453	212	0.3	0.28
W_{5-2}	2392.20	2392.90	3.22	1.59	6.15	0.01	454	191	0.3	0.31

Chapter 3

Wettability Evaluation of East Duvernay Shales and Comparative Analysis of Duvernay Shales Across the Basin

3.1 Materials

3.1.1 Rock Samples

We used 8 pairs of twin core plugs that are drilled from 5 wells (Well 1 to Well 5) located in the ESB. The bulk volume, pore volume, initial mass, and heated mass of the core plugs are listed in **Table A.1**. The pore volume of each core plug is obtained by multiplying its bulk volume by the reported porosity listed in **Table 1**.

Table 4 — Depth, initial mass, bulk volume, pore volume of the twin plugs from ESB

Well	Sample ID	Pair	Core Depth (m)	Initial Mass (g)	Bulk Volume (g)	Porosity (%BV)	Pore Volume (cm^3)
Well 1	W_{1-3}	W_{1-3o}	1973.62	118.7	44.4	1.91	0.849
		W_{1-3w}	1973.62	114.9	42.9	1.91	0.819
	W_{1-4}	W_{1-4o}	1976.57	239.0	89.4	1.24	1.109
		W_{1-4w}	1976.57	238.9	89.4	1.24	1.109
	W_{1-5}	W_{1-5o}	1993.65	102.0	41.1	2.13	0.875
		W_{1-5w}	1993.65	103.5	41.5	2.13	0.884
Well 2	W_{2-1}	W_{2-1o}	2193.58	67.3	26.5	4.72	1.251

		$W_{2\text{-}1w}$	2193.58	62.3	24.5	4.72	1.156
Well 3	$W_{3\text{-}1}$	$W_{3\text{-}1o}$	2223.90	53.7	22.0	6.25	1.375
		$W_{3\text{-}1w}$	2223.90	55.5	40.1	6.25	2.506
	$W_{3\text{-}2}$	$W_{3\text{-}2o}$	2231.10	51.5	19.2	1.91	0.367
		$W_{3\text{-}2w}$	2231.10	63.6	23.7	1.91	0.453
Well 4	$W_{4\text{-}1}$	$W_{4\text{-}1o}$	2314.30	65.7	25.6	2.98	0.763
		$W_{4\text{-}1w}$	2314.30	13.7	5.3	2.98	0.159
Well 5	$W_{5\text{-}1}$	$W_{5\text{-}1o}$	2389.42	41.8	16.9	4.49	0.759
		$W_{5\text{-}1w}$	2389.42	30.6	12.4	4.49	0.555

3.1.2 Fluid Samples

Reservoir oil and produced brine were collected from the cored well. For preparation of fluids used for spontaneous-imbibition tests, the reservoir oil/brine mixture (**Figure 3a**) was separated using a separatory funnel (**Figure 3b**). After 12 hours, the oil was collected at the top of the separatory funnel and was centrifuged at a speed of 3,500 rpm for 20 minutes to remove the heavy components and solid precipitations (**Figure 3c**). The brine was collected at the bottom of the separator funnel and filtered using a 20-micron filter paper (**Figure 3d**). We measured surface tension of the oil and brine, and interfacial tension between the two fluids using a Du Noüy ring tensiometer. We measured viscosity of the fluids by a rotational viscometer. All the tests were conducted at 25°C and atmospheric pressure. **Table 5** lists the properties of reservoir oil and produced brine used for the spontaneous-imbibition tests.

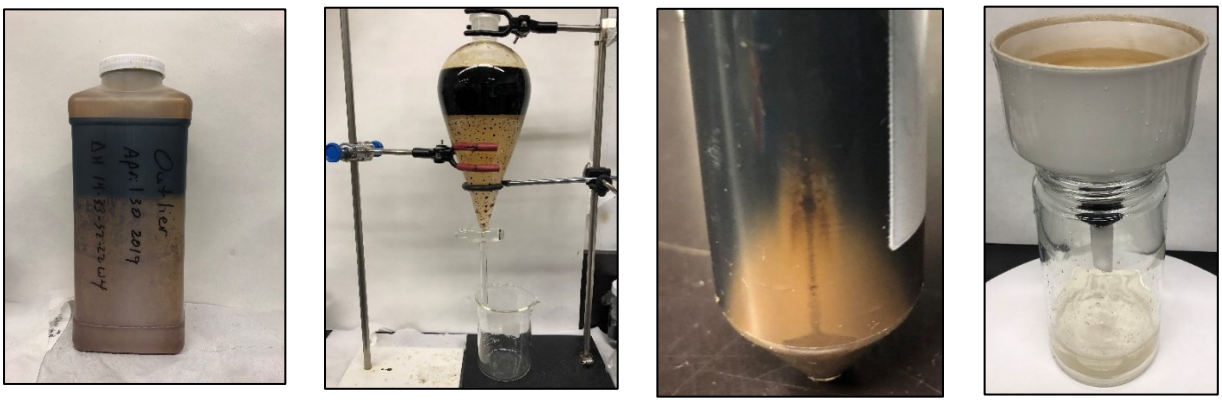

(a) (b) (c) (d)

Figure 3 — Preparation of reservoir fluids (a) oil and brine mixture as received, (b) fluid separation using separatory funnel, (c) impurities at the bottom of tube after oil centrifuge, and (d) Buchner funnel used for brine filtering.

Table 5 — Physical properties of the oil and brine samples used in this study.

Fluid	Density (g/cm^3)	Surface Tension (mN/m)	Viscosity (cP)	Interfacial Tension (mN/m)
Oil	0.845	25.70	28.0	14.71
Brine	1.134	45.06	2.2	

3.2 Methodology

3.2.1 Sample Heating

We heated all as-received core plugs in the oven at 90°C to evaporate the possible initial oil and brine in the pore system to have sufficient pore volume for the imbibition tests. The water

saturation of as-received samples is expected to be relatively low compared with their oil saturation based on the TRA results (**Table 1**). Therefore, the evaporated liquid from the plugs was assumed to be mainly oil. The weight of heated samples was measured over time until reaching the equilibrium conditions. The evaporated oil volume was calculated by dividing weight loss of the heated samples by oil density. It was then normalized by pore volume of the core plugs, calculated from core's bulk volume and the reported porosity data from TRA.

Figure 4 shows oil evaporation profiles of the core plugs used for wettability evaluation. Normalized evaporated volume (Evp_{oil}) is calculated by dividing the evaporated oil volume by core plug's pore volume, obtained from TRA analysis, assuming there is only reservoir oil in the core samples.

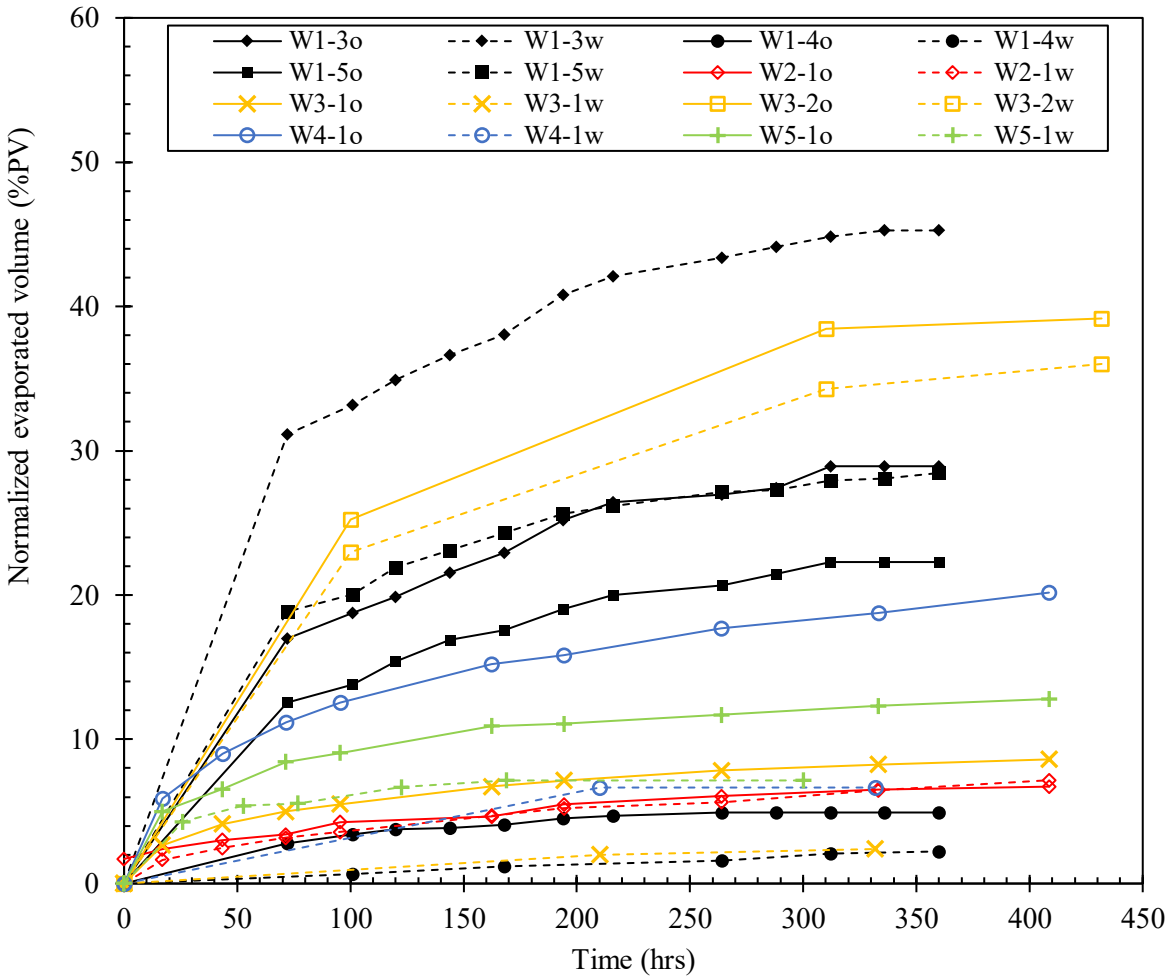

Figure 4 — Normalized evaporated volumes (% Pore volume) versus time. (a) Oil density is used and (b) brine density is used to calculate the evaporated volume. The heating temperature is 90°C.

3.2.2 Comparative Spontaneous Imbibition on Twin Plugs

We conducted comparative spontaneous imbibition tests to evaluate the wetting behavior of ESB samples and the results were compared with those of WSB samples in terms of their petrophysical properties. The as-received core plugs were heated in the oven at 90°C to evaporate the initial oil and brine in the pore system to have sufficient pore volume for the imbibition tests. We conducted oil and brine spontaneous imbibition tests on selected samples from all five wells with varying TOC content and kerogen maturity. The dimensions, bulk volume, and initial mass of all samples were measured before the tests (**Table 2)**. **Figure 5** shows the setup of spontaneous imbibition test. To conduct the imbibition tests, we put a mesh stand in each container, and poured imbibing fluids into the containers to the height of the mesh stand. Then, we placed the plugs on the mesh stand with the bottom face of the plugs in contact with the imbibing fluid. The plug's weight was measured periodically using a weight balance with 1 mg accuracy. The imbibed volume was calculated by dividing the imbibed mass by the liquid density. We normalized imbibed volume through dividing it by bulk volume (BV) and by pore volume (PV) of the plugs. Normalized imbibed volumes of oil and brine at equilibrium conditions were calculated by the equations shown in **Appendix A.4**, and they were used to investigate wettability of the plugs. We also defined oil wettability index (WI_o) using the equation shown in **Appendix A.4**.

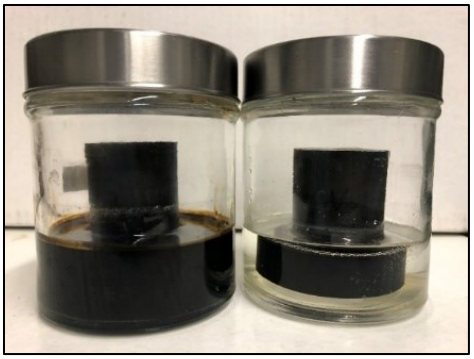

Figure 5 — Oil and brine co-current imbibition tests on $W_{1\text{-}3}$ twin plugs.

3.3 Results and Discussions

3.3.1 Oil and Brine Spontaneous Imbibition on ESB Twin Plugs

Overall, imbibition results presented in this part show that TOC-rich ESB plugs do not necessarily imbibe more oil than brine. Instead of TOC content, kerogen maturity has a positive influence in oil uptake by these plugs. **Figure 6** shows the normalized imbibed volumes of oil vs. time for the selected plugs from each well. **Figure 6** shows that $(I_o^{eq})_{PV}$ for plugs from Well 1 and 2 are less than 5%PV. Well 3, 4, 5 plugs have comparatively higher $(I_o^{eq})_{PV}$ while core plug $W_{3\text{-}2}$ has the highest $(I_o^{eq})_{PV}$ which is 40% followed by $W_{4\text{-}1}$ and $W_{5\text{-}1}$ with $(I_o^{eq})_{PV}$ of 20 and 15%, respectively. **Figure 6a** shows the normalized imbibed volumes of brine vs. time for the ESB plugs indicating preferentially water-wet behavior, while **Figure 6b** shows two particular plugs $W_{4\text{-}1}$ and $W_{5\text{-}1}$ having preferentially oil-wet behavior. Based on the previous studies, TOC content is generally believed to control the organic-pore connectivity in shales where higher TOC content results in

higher oil imbibition (Odusina et al., 2011). Higher oil imbibition of sample $W_{5\text{-}1}$ can be explained by the higher TOC content of 14.45 wt% shown in **Table 1**. However, TOC content for samples $W_{4\text{-}1}$ is only 0.45 wt% which is much lower than TOC content for sample $W_{2\text{-}1}$ and $W_{3\text{-}1}$ which are 3.15 wt% and 5.35 wt%, respectively. The unexpected imbibition results of samples with poor TOC content showing oil-wet behavior can be further analyzed by comparing WI_o of ESB and WSB plugs and evaluating the effect of TOC content and maturity index on oil and brine uptake.

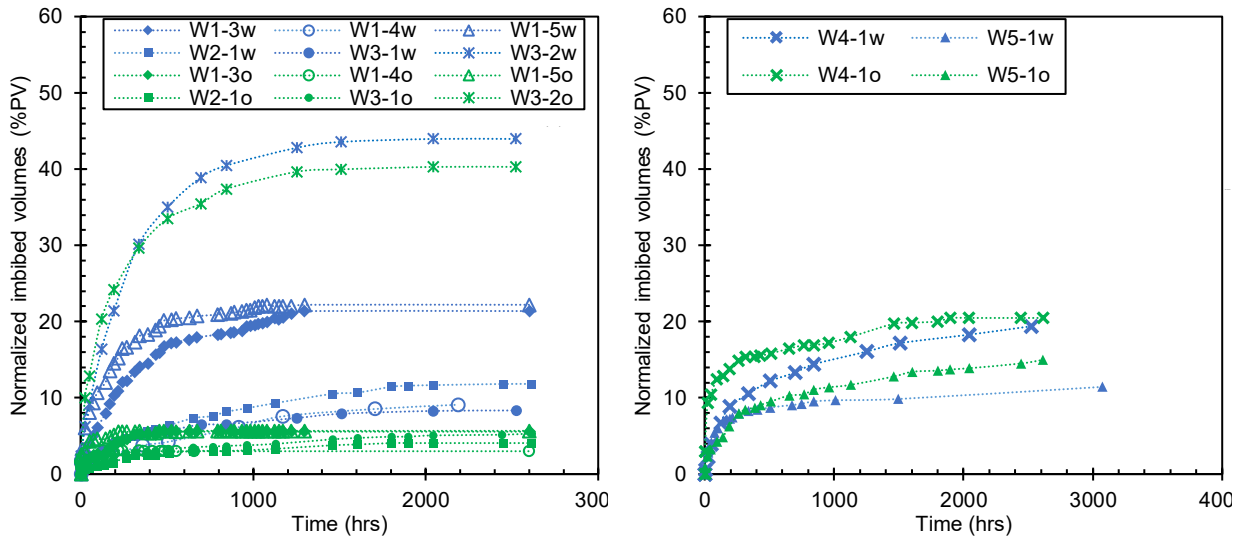

Figure 6 — Imbibed volume of oil and brine vs. time normalized by pore volume for (a) plugs $W_{1\text{-}3}$, $W_{1\text{-}4}$, $W_{1\text{-}5}$, $W_{2\text{-}1}$, $W_{3\text{-}1}$, and $W_{3\text{-}2}$ showing relatively higher wetting affinity to brine; (b) and plugs $W_{4\text{-}1}$ and $W_{5\text{-}1}$ showing relatively higher wetting affinity to oil.

3.3.2 Calculation of Wettability Index and Comparison between ESB and WSB Core Plugs

We calculated WI_o of ESB plugs based on our imbibition results and compared them with those of WSB plugs in terms of their TOC richness. The crossplot of WI_o versus TOC (wt%) of WSB and ESB plugs are shown in **Figure 7**. Overall, WSB plugs have higher WI_o than ESB plugs indicating their stronger affinity to oil. WSB plugs show that WI_o are positively correlated with TOC content while ESB plugs has no obvious correlation. ESB plugs with higher TOC content do not necessarily show higher oil imbibition.

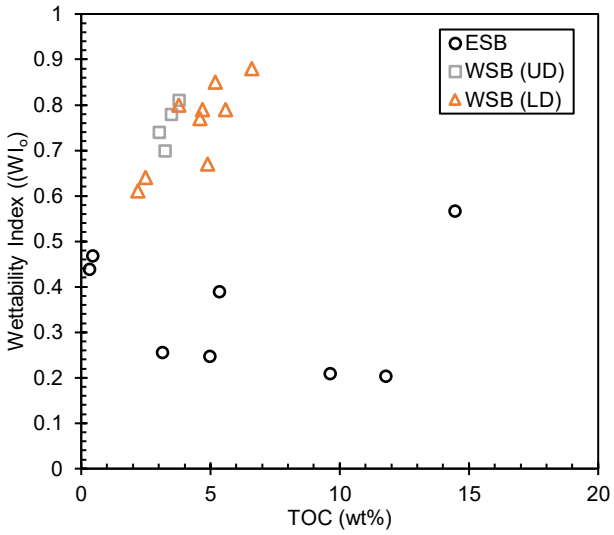

Figure 7 — Crossplot of WI_o vs. TOC (wt%) compared between WSB and ESB samples; WSB samples show positive correlation while WI_o of ESB samples does not show any correlation with TOC content.

3.3.3 Correlations between Imbibition and Production Index and T_{max}

It has been reported that oil generation from source rocks began at "T_{max}" of 435 °C to 465 °C, and production index "PI" between 0.2 and 0.4 (Baskin, 1997). The organic matters are in immature stage when "T_{max}" is less than 435 °C and "PI" is less than 0.2. The gas generation from source rocks starts at "T_{max}" of 470 °C and production index "PI" higher than 0.4 (Baskin, 1997). Since oil uptake by shales depend not only on the amount of OM presents but also the maturity of OM (Luo and Zhong, 2020), we compared WI_o of ESB plugs with their PI and T_{max} which are two indicators of thermal maturation. The crossplot of WI_o versus PI and TOC are shown in **Figure 8a** and **8b**, respectively. Both crossplots show positive slope which indicate a positive correlation between oil uptake and kerogen maturity. **Figure 8b** shows that WI_o are strongly correlated with T_{max} with a R_2 regression of 0.86. Micro- and fine mesopores hosted within organic matter increase with thermal maturity while coarse pores decrease with burial depths due to compaction (Munson, 2015). W_{5-1} is at a depth deeper than W_{2-1} by about 200 meters as shown in **Table 1**. Despite the possible shift in pore size to finer sizes due to compaction, the fine pores developed within organic matter can be sufficiently connected to contribute to higher oil uptake. Both the production index (PI) and T_{max} indicate the level of thermal maturation.

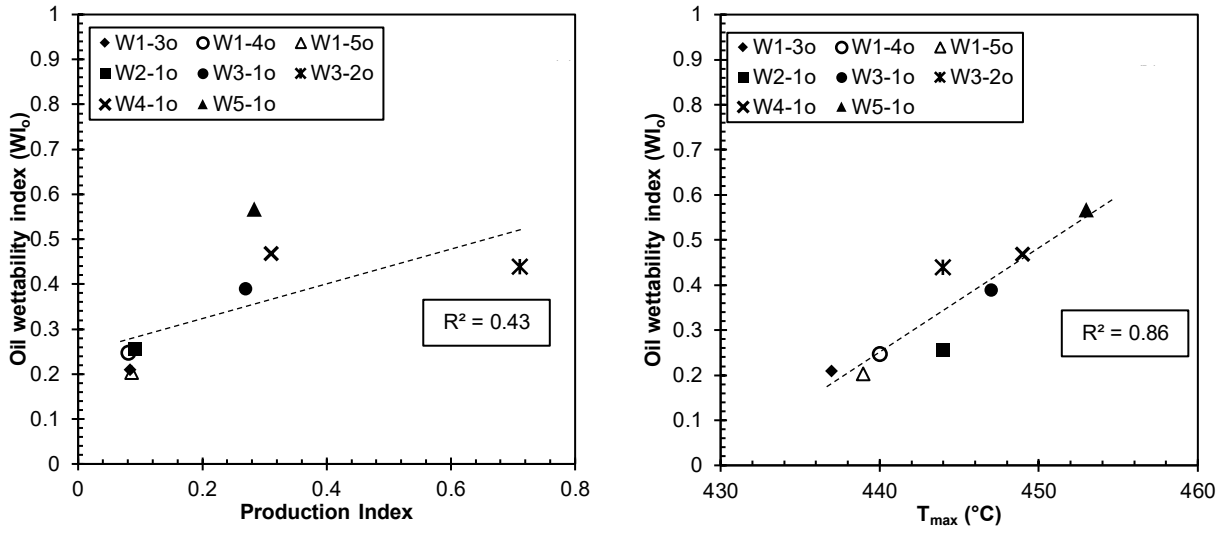

Figure 8 — Crossplot of WI_o vs. (a) production index; and (T_{max}) from rock-eval pyrolysis for ESB plugs.

3.3.4 Comparison between SI Results and Petrophysical Properties of ESB and WSB Samples

The SI test results differ from what we previously observed for the Duvernay samples from WSB showing strongly oil-wet characteristics (Yassin et al., 2017; Begum et al., 2019). Therefore, we compared ESB and WSB samples in terms of their XRD and rock-eval pyrolysis results to investigate the effects of mineralogy, kerogen thermal maturity, and pore connectivity on oil and brine uptake.

The average porosity and permeability of the ESB samples (1.61% and 64.1 nD) is lower than

those of the WSB samples reported in the previous study (3.77% and 167.5 nD) (Yassin et al., 2017; Begum et al., 2019). The average minerology of the 5 ESB samples and that of 17 WSB samples are compared in **Figure 9a** and **9b**, respectively. The WSB samples are quartz rich (45%) with a low calcite content (14%), while the ESB samples are calcite rich (59%) with a low quartz content (13%). The difference in mineralogy, demonstrated in **Figure 9**, is explained by different basinal settings of ESB and WSB. ESB was more isolated, with less open marine circulation than WSB. Shedding of carbonate materials from the Leduc reefs and platform margins surrounding ESB are considered as the main contributors to the formation of the carbonate-rich depositional environment (Marshall et al., 2019). WSB had more connection to the open oceans to the west, leading to more contribution from cratonic-silica source and more diversity in the fauna including silica-shelled organisms. Carbonate content is less in WSB especially as we get farther from the reefs. There is also more clay content in WSB due to the same factors.

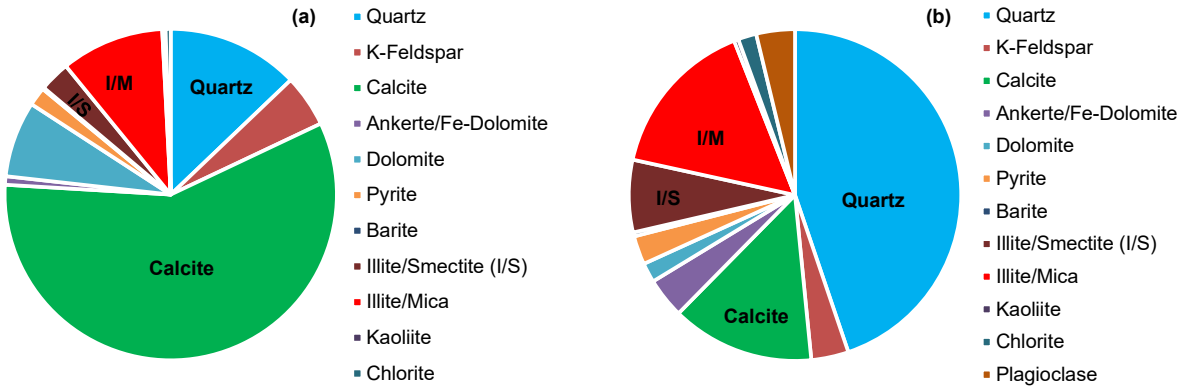

Figure 9 — Comparing the average minerology of the offset samples from (a) East Shale Basin, and (b) West Shale Basin. I/M and I/S stand for Illite/Mica and Illite/Smectite, respectively.

Figure 10a and **10b** compare the rock-eval pyrolysis results of ESB and WSB samples. Average TOC content of the ESB samples is 5.5 wt% which is higher than that of WSB samples with an average TOC content of 3.8 wt%. Having TOC content greater than 4.0 indicates that the samples are excellent source rocks in terms of hydrocarbon potential (Baskin 1997). HI and TOC content of ESB samples are significantly higher than those of WSB samples. ESB was surrounded by the carbonate reefs/platforms and there were restricted circulation currents, resulting in less quartz and clay deposition. The anoxic environment resulting from the lack of circulation is believed to be the reason for the higher preservation of organic matter and elevated level of HI in the ESB deposits. In contrast, stronger circulation currents in WSB with more open marine conditions result in less anoxic environment and less preservation of organic matter. **Figure 10a** shows that average T_{max} of ESB is 442°C which is lower than average T_{max} of 479°C for the WSB samples. This is consistent with higher thermal maturity of WSB samples compared with that of ESB samples since T_{max} indicates thermal maturity.

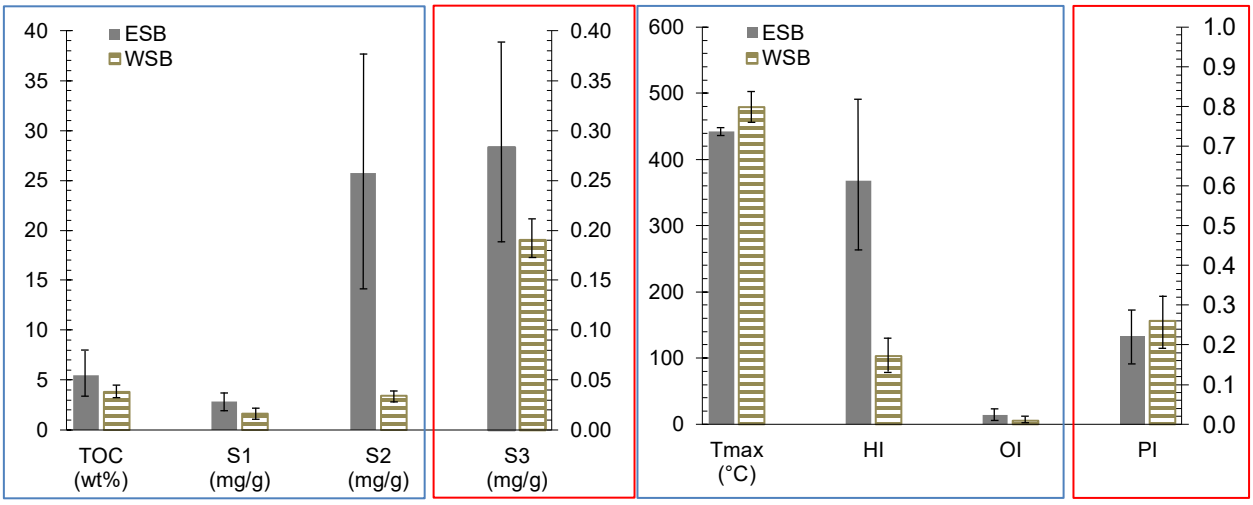

Figure 10 — Comparing average value of rock-eval pyrolysis results for ESB and WSB samples. (a) TOC content, S_1, S_2, and S_3 and (b) T_{max}, HI, OI, and PI.

3.3.5 Driving Forces for Brine Imbibition

Inorganic-pore connectivity. $(I_w^{eq})_{PV}$ values of ESB plugs are up to 44%. Unlike WSB having quartz-rich characteristics, the samples in this study are categorized as calcareous shales. Inorganic minerals such as calcite, quartz, and clays can be hydrophilic in the presence of air, and organic matter tends to be hydrophobic (Schrader and Yariv, 1990; Hakim et al., 2017; Yassin et al., 2017). **Figure 9** shows that ESB plugs have high average calcite content of 60 wt% compared to WSB samples with an average calcite content of 14%. The higher calcite content of ESB samples can also be confirmed by their SEM images shown in **Figure 15**. **Figure 15e** and **15f** show SEM images of $W_{1\text{-}1}$ with pores bordered by inorganic minerals mainly composed of calcite and clays. These pores may generate inorganic conduits which can contribute to water uptake by shales (Yang et al., 2019). The higher water imbibition compared to oil imbibition observed in **Figure 6** can be explained by the abundance of these inorganic pores.

Osmotic pressure due to salinity gradient. ESB plugs used for imbibition tests were not cleaned with any solvents, possible salts precipitation from reservoir brine inside the pore network can cause a chemical potential difference between the imbibed water and external water due to salts dissolution. This chemical potential difference can act as the osmotic pressure for additional water uptake, explaining preferentially water-wet behavior of the ESB samples (Chenevert, 1989; Xu

and Dehghanpour, 2014). **Figure 11a** and **11b** show SI results of brine and DI-water into sample $W_{5\text{-}1}$ and $W_{5\text{-}2}$. DI-water has higher imbibed volume than brine in sample $W_{5\text{-}1}$. Sample $W_{5\text{-}1}$ shows a more rapid DI-water imbibition than brine in the first 200 hours. The electrical conductivity of DI-water is also recorded and shown in **Figure 12**. As DI-water imbibes, salts presented in the core plug can be dissolved in the imbibing water. Higher salinity gradient can lead to higher driving force for DI-water imbibition.

Water adsorption by clays. Water adsorption by clay minerals which is driven by chemical potential difference and the nature of clay structure can also lead to water uptake (Xu and Dehghanpour, 2014). The ESB samples have an average clay content of 15 wt%. The negative charge of clays and cations in solution form an electrical double layer which imposes a negatively-charged medium. Positively-charged ions and polar water tend to be attracted by negatively-charged clay surface (Chenevert, 1989), leading to more water uptake by the ESB plugs.

Induced microfractures by clay expansion. Clay platelets are close together when dehydrated. As water molecules adsorbs to negatively-charged surface of clay platelets, the adsorption of water molecules develops internal stresses that cause the platelets to separate (Chenevert, 1970). Microfractures can be induced due to the expansion of the clays (Dehghanpour et al., 2013). Induced microfractures can increase the permeability for brine imbibition.

It is important to mention that osmotic pressure, water adsorption by clays, and induced microfractures due to clay swelling are absent in the case of oil imbibition which can explain the relatively lower imbibed volume of oil compared to imbibed volume of brine (**Figure 6**).

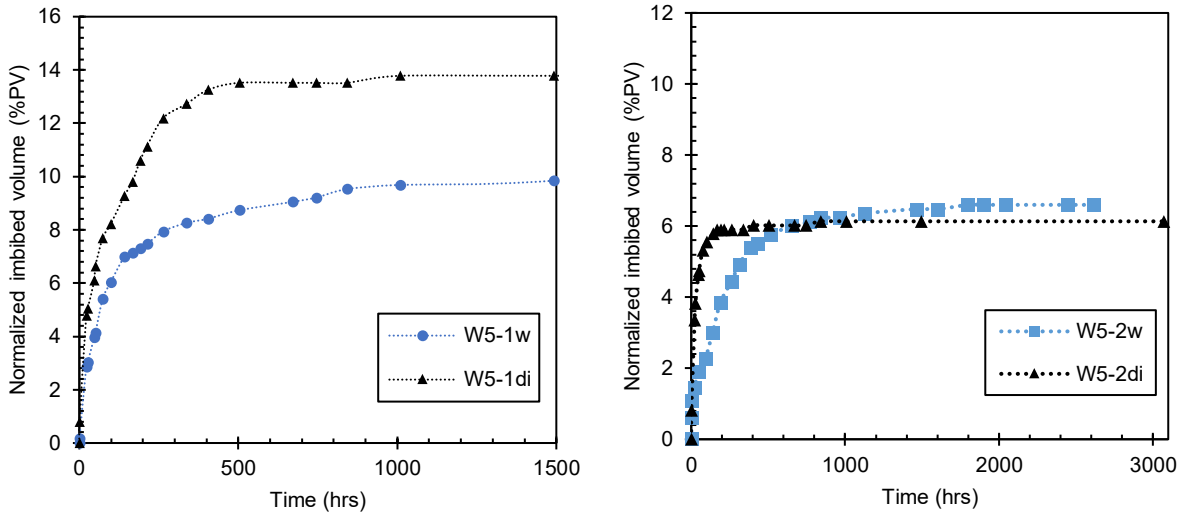

Figure 11 — Imbibed volume of brine and DI-water vs. time for plugs (a) $W_{5\text{-}1}$ and (b) $W_{5\text{-}2}$, normalized by pore volume.

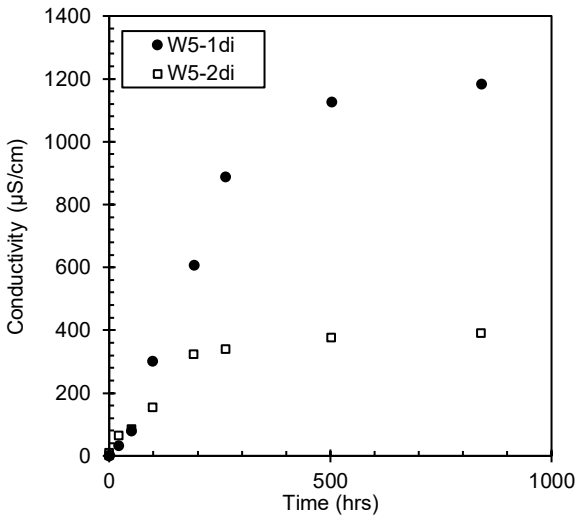

Figure 12 — Electrical conductivity of external DI-water vs time during SI measured by using electrical conductivity meter.

Chapter 4

Investigating the Effect of Kerogen Maturity on Pore Structure of ESB Plugs

4.1 Sample Preparation and Methodology

4.1.1 Low-Pressure Nitrogen Gas Sorption Test

Low-pressure gas sorption test (LPGS) was performed on a Quantachrome Autosorb MP1 using N_2 at 77 K (-196°C). Adsorption and desorption isotherms were run over a P/P_o range of 0.01 to 0.99. Pore size distribution were determined by the density function theory (DFT) method. Prior to any measurements, the samples were placed in a 9 mm glass rod to be degassed in a vacuum at room temperature for 20 hours to remove water.

4.1.2 Scanning Electron Microscopy (SEM) and Energy Dispersive Spectroscopy (EDS) Analyses

Scanning electron microscopy (SEM) and energy dispersive spectroscopy (EDS) analyses were conducted to study the size, morphology, and spatial distribution of pores. We cut the rock samples into 1cm x 1cm thin sections with the thickness of 5 to 8 mm. The thin sections were mechanically polished with grinder, polisher, and sand papers with Grade P400, P800, P1200, and P2400, sequentially. We polished the samples for 10 to 15 minutes at each step. The polished samples were ion milled at an accelerating voltage of 8.0 kV and a current of 3.0 mA for 1 hour to further

reduce the surface roughness. Then, we coated the samples with a layer of conductive carbon with the thickness of 5 to 6 nm to reduce the charging effects. Finally, SEM images were taken with an accelerating voltage of 15 keV at a typical working distance of 8.5 mm. The EDS analyses were conducted on SEM images to identify the mineral compositions of the samples at the pore scale.

4.2 Results

4.2.1 N_2 Sorption Isotherm

N_2 sorption isotherms from BET analysis form a hysteresis loop with a characteristic shape illustrated in **Figure 13**. The hysteresis indicates that a portion of the N_2 adsorbed can not be desorbed during the desorption process. N_2 is an inert gas and it can condense in both hydrophobic and hydrophilic pores. The shapes of curves shown in **Figure 13** suggest Type II hysteresis loop which can be interpreted as micropore filling at low relative pressure and the curvature increases rapidly near P/P_o =1 due to the presence of macropores (Labani et al., 2013). Gas adsorption at low relative pressure is correlated with micropores and small mesopores, while at high relative pressure is correlated with large mesopores and macropores. **Figure 13c** shows that $W_{5\text{-}1}$ plug has the lowest volume of N_2 adsorbed by larger pores at high relative pressures than $W_{4\text{-}1}$ followed by $W_{1\text{-}4}$ plug shown in **Figure 13b** and **13a**. This can be interpreted as lower volume of larger pores being presented as maturity level increases.

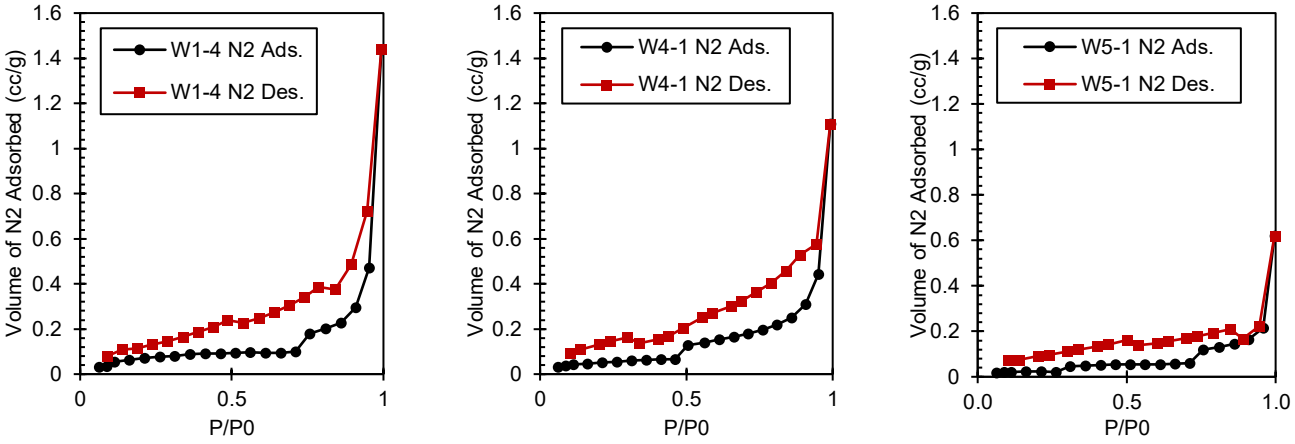

Figure 13 — N_2 sorption isotherms measured by BET for (a) $W_{1\text{-}4}$, (b) $W_{4\text{-}1}$ and (c) $W_{5\text{-}1}$ samples. Adsorption and desorption isotherms are plotted in black and red colors, respectively.

4.2.2 DFT/Monte-Carlo Pore Volume Histogram

To quantify PSDs of these samples, we plot their pore volume histograms calculated by DFT method shown in **Figure 14**. We used the classification scheme proposed by International Union of Pure and Applied Chemistry to characterize the porosity of the samples. The widths of macropores, mesopores, and micropores are approximately greater than 50 nm, between 50 and 2 nm, and less than 2 nm, respectively. (Munson, 2015). We see a higher proportion of pores within the coarse mesopore (>10 nm) in $W_{1\text{-}4}$ (**Figure 14a**). They progressively decrease in volume toward smaller pore diameters in more matured $W_{4\text{-}1}$ and $W_{5\text{-}1}$ plugs shown in **Figure 14b** and **14c**, respectively. The pore volume distribution indicates a minimal volume of N_2-accessible fine mesoporosity within immature samples. Oil window samples contain relatively greater volumes of fine mesopores. Fine mesopores (< 10 nm), as measured by N_2 low-pressure sorption analysis,

is developed systematically with maturity which reflects the generation of fine pores hosted within organic matter. Simultaneously, coarse mesopores (> 10 nm) and macropores (> 50 nm) undergo a progressive loss of pore volume due to compaction effects. This is interpreted in **Figure 13c** whereas $W_{5\text{-}1}$ plug with the highest depth has the smallest increase at high relative pressure among all three samples. The increase at high relative pressure corresponds to capillary condensation at larger pores.

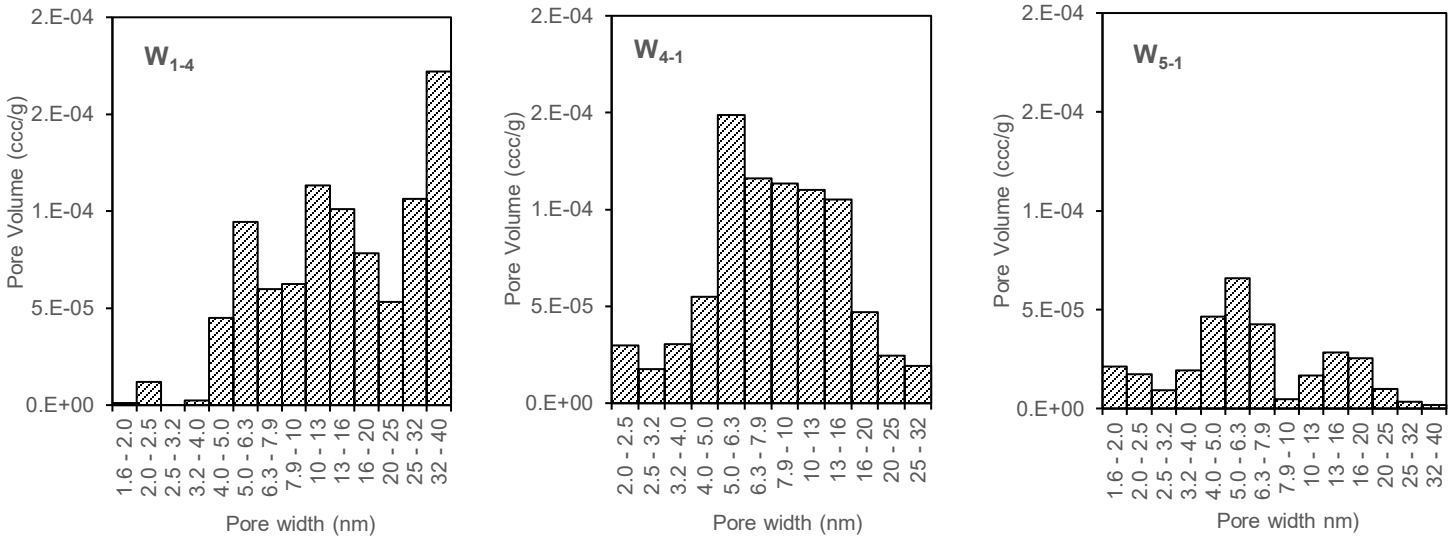

Figure 14 — Pore volume histogram determined by DFT method for (a) $W_{1\text{-}4}$, (b) $W_{4\text{-}1}$ and (c) $W_{5\text{-}1}$ samples.

4.2.3 SEM/EDS Analysis

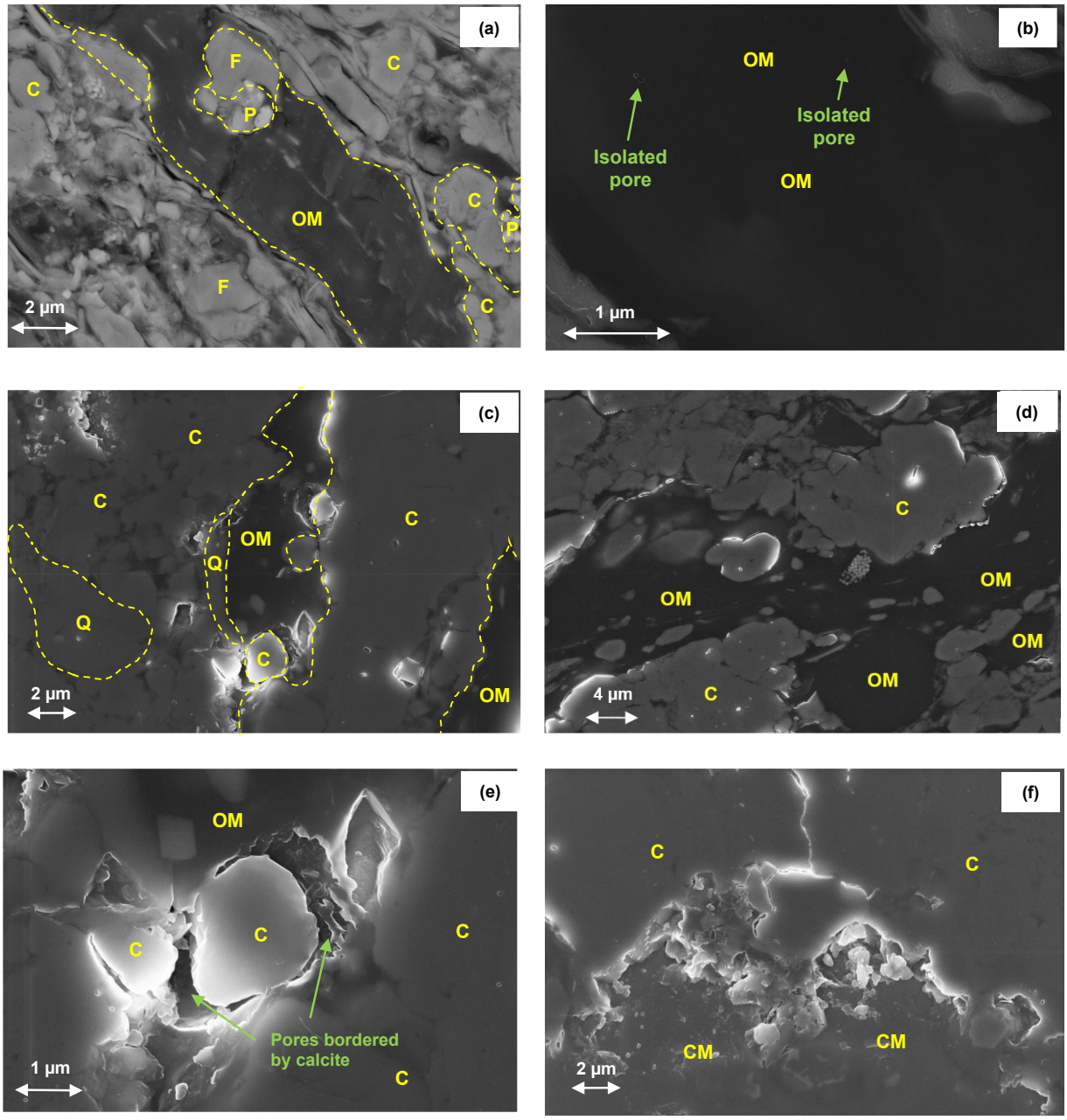
(a)
F
C
C
P
OM
C
P
F
C
2 µm
(b)
OM
Isolated pore
Isolated pore
OM
1 µm
(c)
C
C
OM
C
Q
Q
C
2 µm
OM
(d)
C
OM
OM
OM
OM
4 µm
C
(e)
OM
C
C
C
Pores bordered by calcite
1 µm
C
(f)
C
C
CM
CM
2 µm

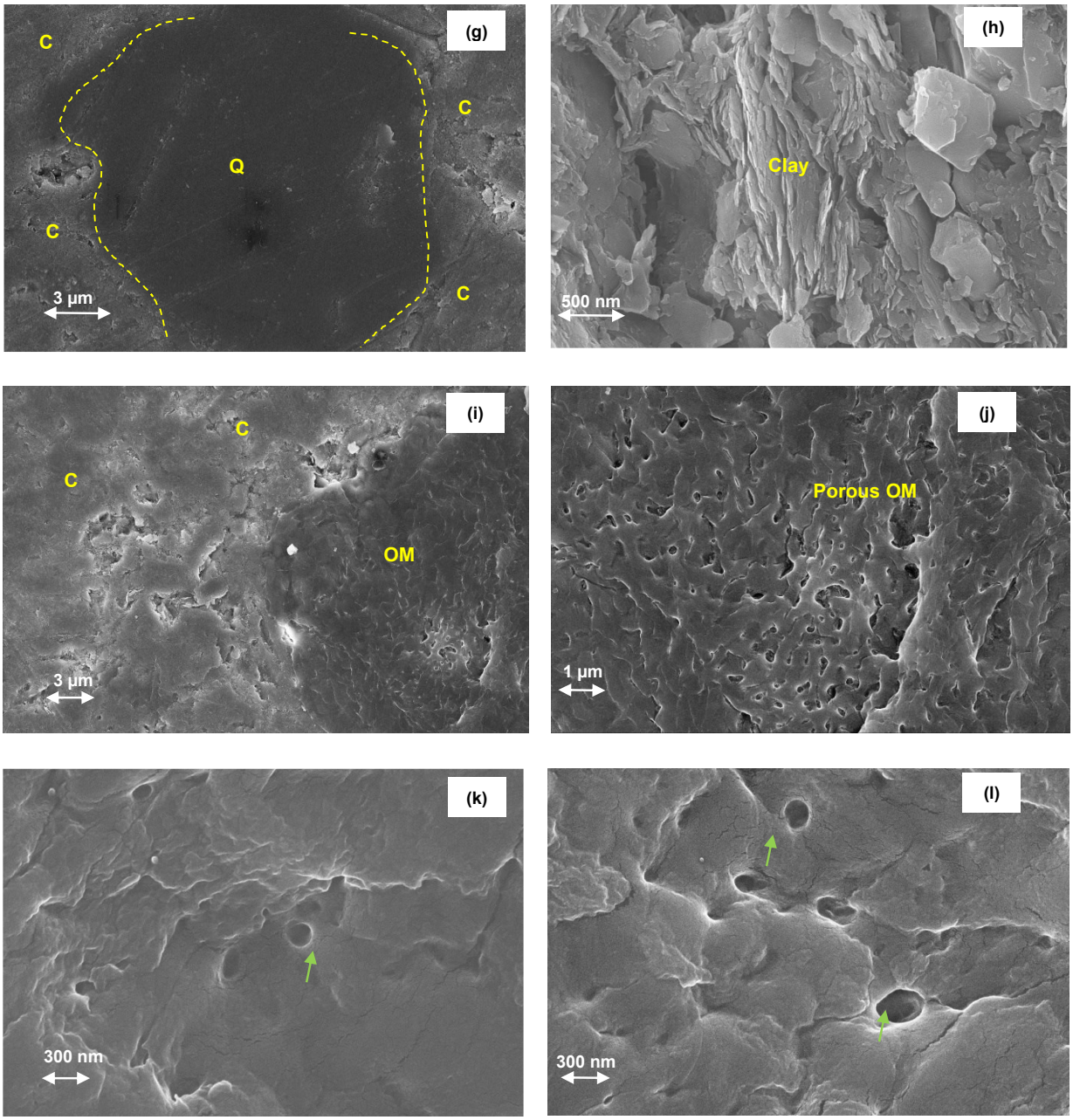

Figure 15 — SEM images of samples (a) $W_{1\text{-}2}$, (b) $W_{1\text{-}9}$, (c) $W_{1\text{-}1}$, and (d) $W_{1\text{-}5}$ showing low number of pores within organic matter; samples (i) $W_{4\text{-}1}$, (j) $W_{4\text{-}1}$, (k) $W_{2\text{-}1}$, and (l) $W_{2\text{-}1}$ showing porous OM;

and sample (e) $W_{1\text{-}1}$, (f) $W_{1\text{-}1}$, (g) $W_{5\text{-}1}$, and (h) $W_{3\text{-}1}$ showing inorganic pores bordered by different inorganic minerals (mainly composed of calcite and clays). OM, C, F, Q, CM, and P represent organic matter, calcite, feldspar, quartz, clay minerals, and pyrite, respectively.

4.3 Discussions

4.3.1 Effect of Kerogen Thermal Maturity

Figure 10a and **10b** compare rock-eval pyrolysis results of ESB and WSB samples. Average S_2 (26 mg/g) of ESB samples is higher than average S_2 (3.5 mg/g) of WSB samples. Higher S_2 indicates that more hydrocarbons are generated through thermal cracking of non-volatile organic matter in ESB samples compared with that in WSB samples. This means that ESB samples would have a good production potential if maturation process had continued (Stoakes, 1980). However, lower T_{max} of ESB samples demonstrates their lower maturity level compared with WSB samples. ESB samples belong to early-oil window, while WSB samples belong to oil and gas windows.

Kerogen wettability depends on its thermal maturity which may affect rock's wettability. Recent studies also suggest kerogen may be mixed-wet or water-wet at low thermal maturities (Hu et al., 2016; Jagadisan and Hedari, 2019). Jagadisan and Heidari. (2019) experimentally demonstrated that kerogen wettability varies with thermal maturity. They heated kerogen from organic-rich mudrocks at different temperatures and measured air/water contact angles on the surface of kerogen with different maturity levels. Their results show that the contact angle of water increases

as kerogen becomes more mature which demonstrate that kerogen wettability is a function of its thermal maturity. Thus, the stronger wetting affinity of ESB samples from early-oil window to brine may be explained by their low thermal maturity.

4.3.2 Effect of Organic-Pore Connectivity

Insignificant imbibed oil volume of ESB samples may indicate that the organic-pore network is poorly connected (Lan et al., 2015). Previous imbibition tests on the Horn River Shales show water-wet behavior of intact samples (Xu and Dehghanpour, 2014), suggesting poor connectivity of the oil-wet pore network. TOC content is generally believed to control the organic-pore connectivity in shales where higher TOC content results in higher oil imbibition (Odusina et al., 2011; Yang et al., 2019). However, recent studies suggest that oil transport not only depends on the amount of TOC but also depends on kerogen thermal maturity since the organic-pore connectivity can be attributed to the pores generated within the OM (Luo and Zhong, 2020; Zhang et al., 2020).

Well-connected organic pores are more abundant in samples with higher thermal maturity level (Cao et al., 2015; Luo and Zhong, 2020). Munson (2015) analyzed SEM images of early-oil window samples of the Duvernay Formation and observed non-porous organic matter. The SEM images of our ESB samples show similar observations. **Figure 15a** through **15d** show the existence of OM in SEM images of $W_{1\text{-}1}$, $W_{1\text{-}2}$, and $W_{1\text{-}5}$ samples. Organic pores are hardly observed within OM of these ESB samples. Pore formation within the OM of source rocks is the result of kerogen

thermal maturation and its conversion to hydrocarbons (Loucks et al., 2010). According to **Figure 2b** and **10b**, the ESB samples experienced low kerogen conversion with average PI of 0.08, while the WSB samples have an average PI of 0.27. The lower number of organic pores in the less-mature ESB samples may be explained by the fact that less pores have been generated during thermal maturation process. This can be confirmed by the SEM images in **Figure 15a** through **15d** where only limited number of pores are observed within OM of the samples. In samples with higher maturity, pores found within OM are both greater in size and abundance. This is shown by the SEM images in **Figure 15i** through **15l** where porous OM is found in samples from oil window.

The abundance of well-connected pores in OM controls the wetting behavior of shale samples (Begum et al., 2019). Such pores in WSB samples create hydrophobic pathways for oil imbibition which can explain their strong wetting affinity to oil. In contrast, ESB samples from early-oil window have fewer connected organic pores within OM. Despite their higher TOC content (5.5 wt%) compared to WSB samples (3.8%), the organic matter of ESB samples is not porous enough to create hydrophobic conduits for oil imbibition.

Chapter 5

Investigating the Role of Fracture on Oil Uptake by ESB Core Plugs

5.1 Materials and Methodology

5.1.1 Characterization of Fractures of ESB Core Plugs Based on CT Scan Images

Table 6 shows the depth, initial mass, bulk volume, and pore volume of the fractured plugs from Well 1 in ESB. These plugs with different types and intensities of fractures were selected to study the effect of fractures on oil imbibition.

Table 6 — Depth, initial mass, bulk volume, pore volume of the fractured plugs from ESB

Sample ID	Core Depth (m)	Initial Mass (g)	Bulk Volume (cm3)	Porosity (%BV)	Pore Volume (cm^3)
$W_{1\text{-}1}$	1970.4	104.6	42.1	1.49	0.63
$W_{1\text{-}2}$	1972.1	185.9	77.0	5.42	4.17
$W_{1\text{-}3}$	1973.6	118.7	44.4	1.91	0.85
$W_{1\text{-}4}$	1976.6	239.0	89.4	6.32	5.65
$W_{1\text{-}5o}$	1993.7	102.0	41.1	2.13	0.87
$W_{1\text{-}6o}$	1997.0	93.7	42.2	2.34	0.99
$W_{1\text{-}7a}$	1999.2	134.3	56.4	5.22	2.95
$W_{1\text{-}7b}$	1999.2	77.0	31.1	5.22	1.62
$W_{1\text{-}9o}$	2004.7	41.2	17.8	1.85	0.33
$W_{1\text{-}10}$	2015.5	241.283	86.3	2.92	2.52

Figure 16a through **16i** show CT scan of all 9 core plugs used for imbibition tests to investigate their fracture intensity. **Figure 16a** and **16g** show 1) open fractures and 2) filled natural fractures (FNF) that for example are represented by white veins in samples $W_{1\text{-}1}$ and $W_{1\text{-}7}$. The open fractures may be reactivated natural fractures or induced fractures due to unloading during the coring operation. The two fracture systems intersect each other and the intersection is at right angle in some cases. Similar fracture systems are also observed in **Figure 17a** and **17b**, showing the full-core images related to samples $W_{1\text{-}1}$ and $W_{1\text{-}7}$, respectively.

Core plugs $W_{1\text{-}1}$ and $W_{1\text{-}7}$ are characterized as highly-fractured (HF) plugs. Core plug $W_{1\text{-}7}$ was cut into $W_{1\text{-}7a}$ and $W_{1\text{-}7b}$ to generate two HF plugs. **Figure 16b**, **16f**, and **16h** show CT scan of $W_{1\text{-}2}$, $W_{1\text{-}6}$, and $W_{1\text{-}9}$ core plugs, respectively. These three samples only show open fractures and no FNF (white veins) was detected. We characterized them as slightly-fractured (SF) plugs. Core plugs $W_{1\text{-}3}$, $W_{1\text{-}4}$, $W_{1\text{-}5}$, and $W_{1\text{-}10}$ are characterized as non-fractured (NF) plugs.

We selected NF plugs of $W_{1\text{-}3}$ and $W_{1\text{-}5}$ as well as SF plugs of $W_{1\text{-}6}$ and $W_{1\text{-}9}$ for wettability evaluation by conducting comparative oil and brine imbibition tests. Samples $W_{1\text{-}1}$, $W_{1\text{-}2}$, $W_{1\text{-}4}$, $W_{1\text{-}7a}$, $W_{1\text{-}7b}$, and $W_{1\text{-}10}$ with various degrees of fracture intensity were selected for oil-imbibition tests.

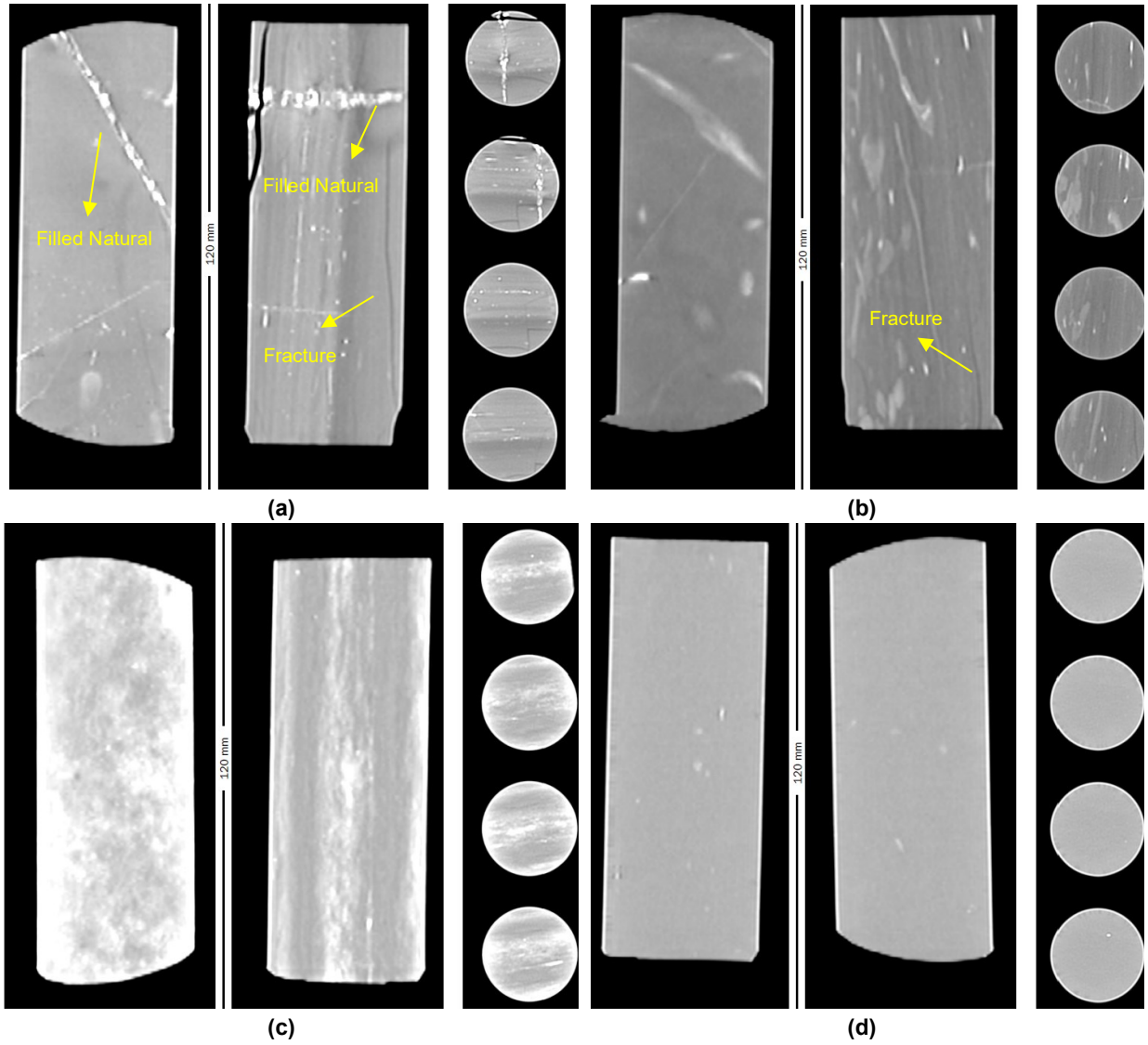
Filled Natural
120 mm
Filled Natural
Fracture
(a)
120 mm
Fracture
(b)
120 mm
(c)
120 mm
(d)

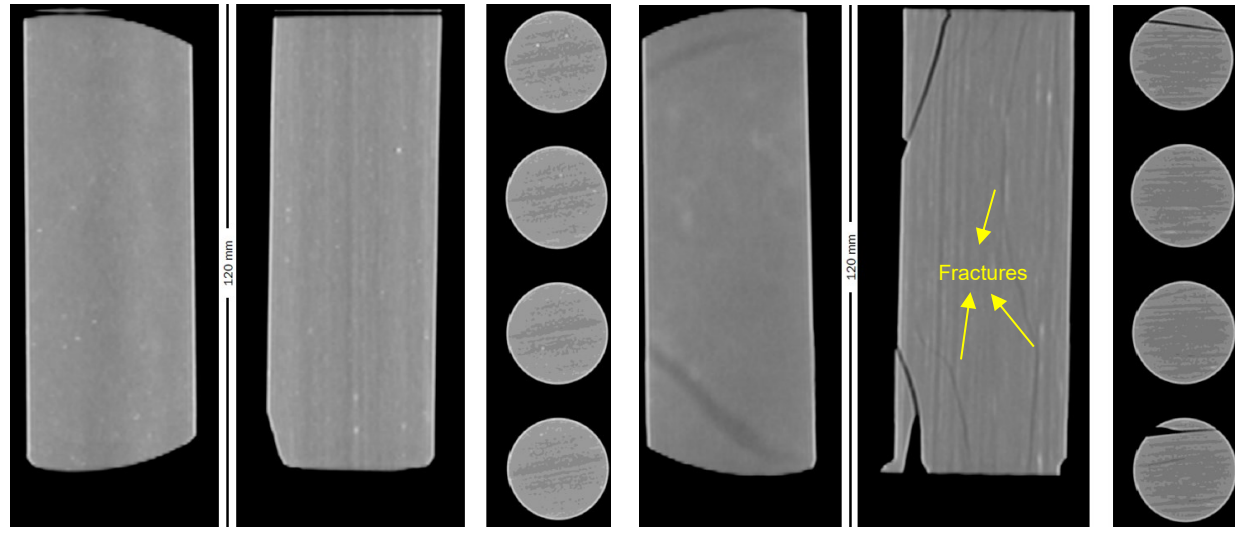
120 mm
Fractures
120 mm

(e) (f)

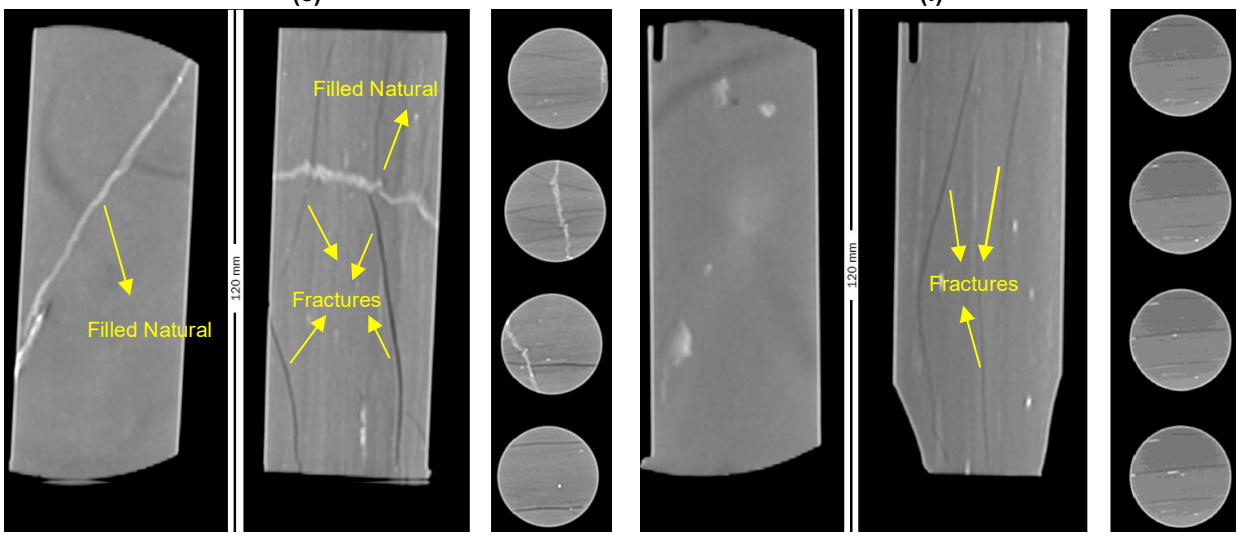
Filled Natural
120 mm
Filled Natural
Fractures
120 mm
Fractures

(g) (h)

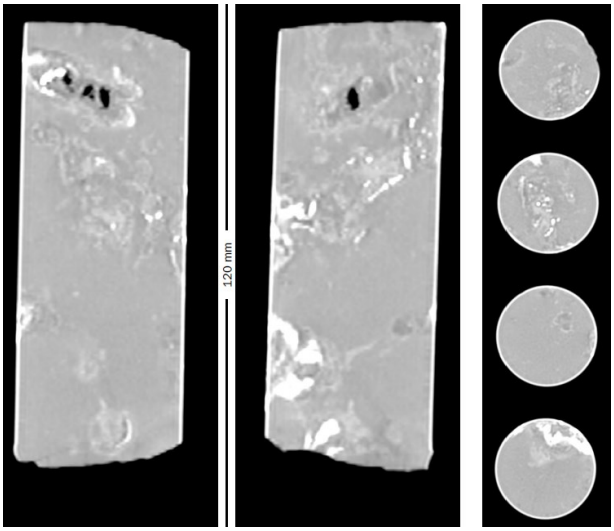

(i)

Figure 16 — CT scan of (a) $W_{1\text{-}1}$, (b) $W_{1\text{-}2}$, (c) $W_{1\text{-}3}$, (d) $W_{1\text{-}4}$, (e) $W_{1\text{-}5}$, (f) $W_{1\text{-}6}$, (g) $W_{1\text{-}7}$, (h) $W_{1\text{-}9}$, and (i) $W_{1\text{-}10}$.

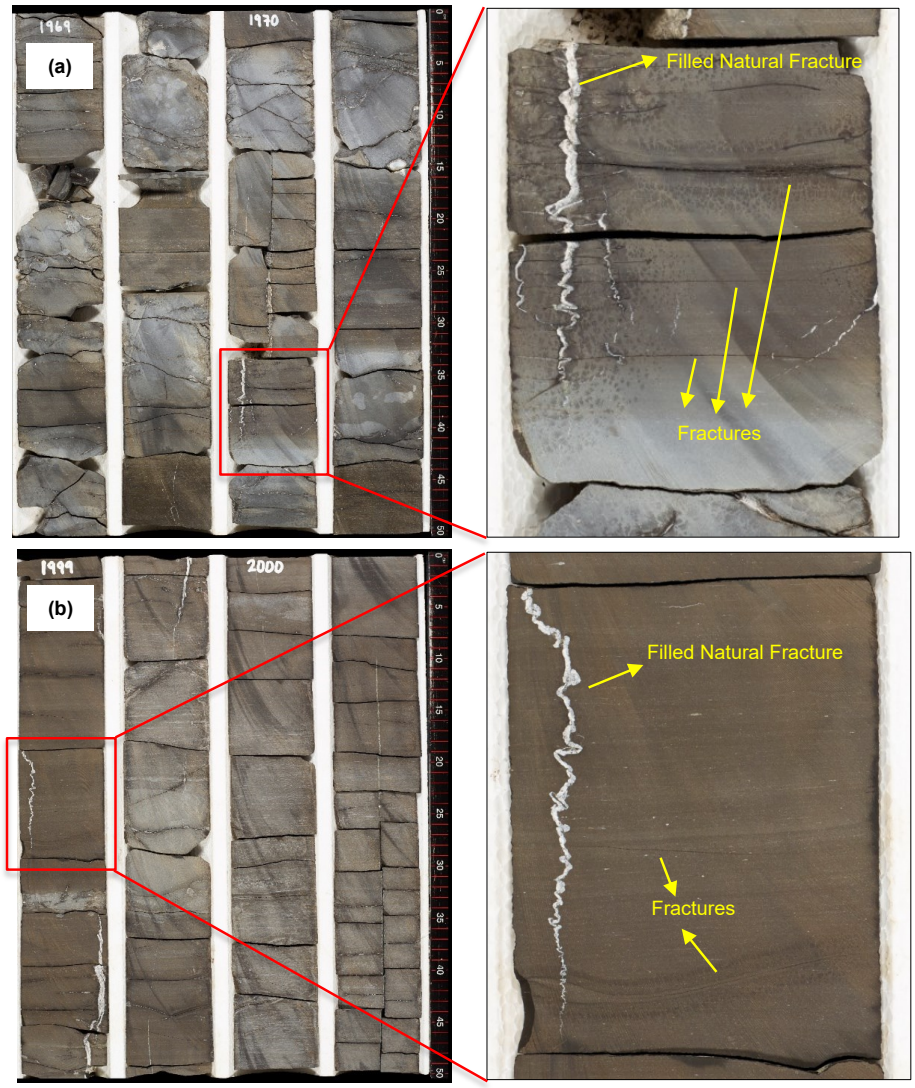

Figure 17 — Full core plug images of (a) $W_{1\text{-}1}$ (1970.42 m) and (b) $W_{1\text{-}7}$ (1999.15 m). The images of highly-fractured (HF) $W_{1\text{-}1}$ and $W_{1\text{-}7}$ plugs show the intersection of open and filled natural fractures (FNF) mostly at right angle.

Table 7 — Characterizing fracture intensity of the ESB plugs based on the CT scan results.

Sample ID	Degree of fracture intensity
$W_{1\text{-}3}$	Non-fractured (NF)
$W_{1\text{-}4}$	Non-fractured (NF)
$W_{1\text{-}5}$	Non-fractured (NF)
$W_{1\text{-}10}$	Non-fractured (NF)
$W_{1\text{-}2}$	Slightly fractured (SF)
$W_{1\text{-}6}$	Slightly fractured (SF)
$W_{1\text{-}9}$	Slightly fractured (SF)
$W_{1\text{-}1}$	Highly fractured (HF)
$W_{1\text{-}7a}$	Highly fractured (HF)
$W_{1\text{-}7b}$	Highly fractured (HF)

5.1.2 Sample Heating of ESB Core Plugs with Different Degree of Fractures

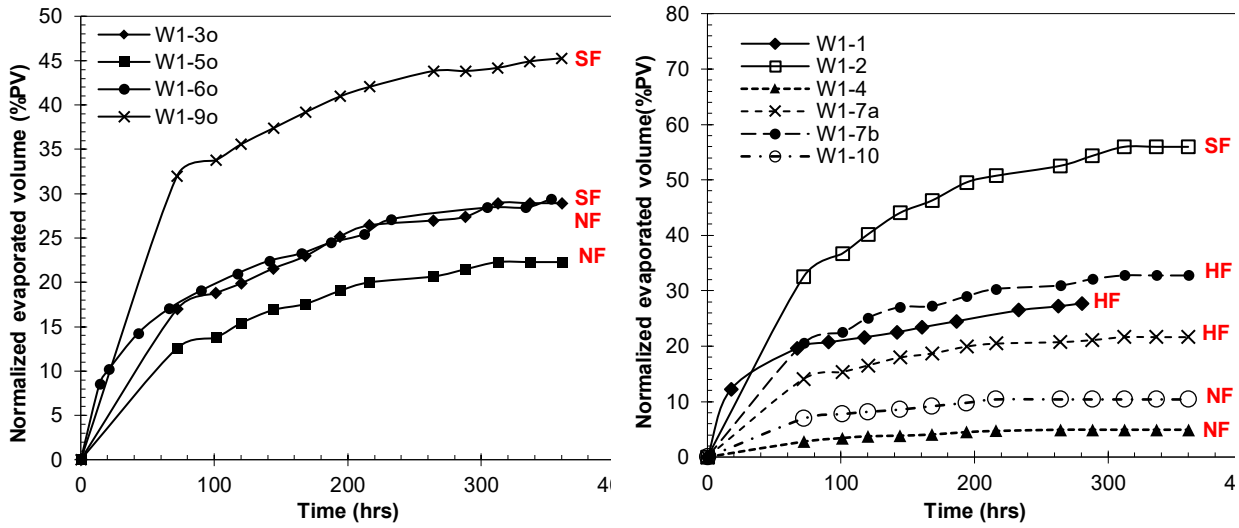

Figure 18 — Normalized evaporated oil volume (Evp_{oil}) vs. time for two sets of core plugs prepared

for (a) comparative oil/brine imbibition tests and (b) oil imbibition tests. Subscripts o and w represent oil and brine, respectively.

5.2 Results and Discussions

5.2.1 Oil Imbibition Results on ESB Core Plugs with Different Degree of Fractures

In this subsection, a total of 6 plugs with various degrees of fracture intensity were selected for oil imbibition tests to investigate the effects of fractures on rock/fluid interactions. $W_{1\text{-}1}$, $W_{1\text{-}7a}$, and $W_{1\text{-}7b}$ are characterized as HF, $W_{1\text{-}2}$ is characterized as SF, and $W_{1\text{-}4}$ and $W_{1\text{-}10}$ are characterized as NF plugs based on the CT scan images (**Figure 16**).

Spontaneous Imbibition of Oil. **Figure 19a** shows imbibed volume of oil normalized by PV with respect to time. HF plugs have the highest imbibed oil volume, followed by the SF and NF plugs, respectively. **Figure 19b** shows the profiles of imbibed volume normalized by BV and the results clearly show the effects of fracture intensity. Comparing **Figure 19a** with **19b** indicates that the effects of fractures are more pronounced when the imbibed volume is normalized by BV. Estimating PVs by the measured porosity of crushed shale samples (**Table 1**) may lead to inconsistent normalized imbibed volumes. In the next section, we will discuss the limitations of crushed-shale helium porosimetry technique for measuring porosity of shale samples with poorly-connected pore network.

We normalized the equilibrated imbibed oil volumes by both PV and BV of the samples and compared them in **Figure 20a** and **20b**, respectively. According to **Figure 20a**, $(I_o^{eq})_{PV}$ is

positively correlated to fracture intensity. This observation indicates that in addition to inorganic porosity (**Figure 15e** to **15h**), fracture intensity plays an important role in the imbibition process. Intersection of open and filled natural fractures in $W_{1\text{-}1}$ and $W_{1\text{-}7}$ plugs (**Figure 17**) enhances their pore connectivity, leading to significantly higher imbibed volume of oil in these plugs.

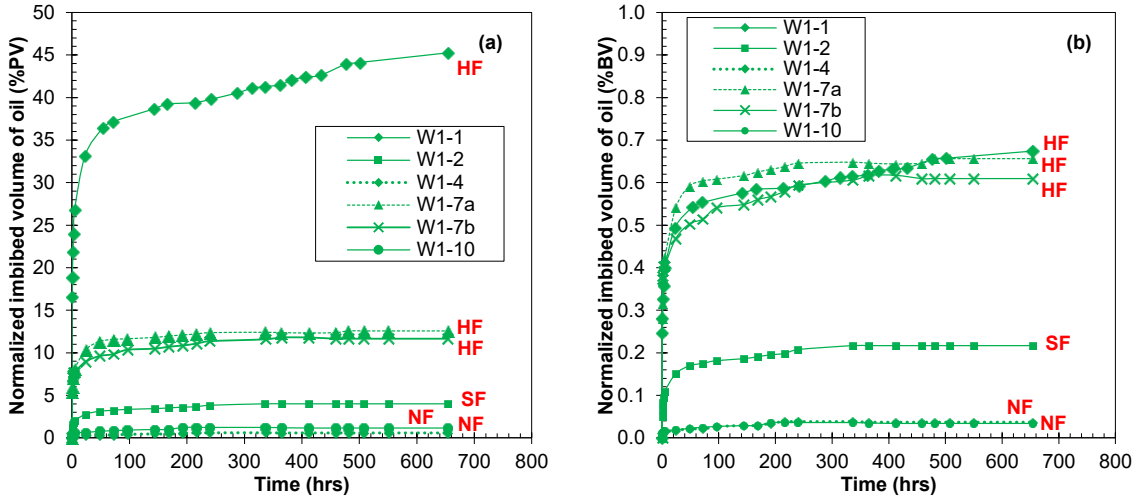

Figure 19 — Normalized imbibed volume of oil vs. time (a) normalized by pore volume (PV) and (b) normalized by bulk volume (BV).

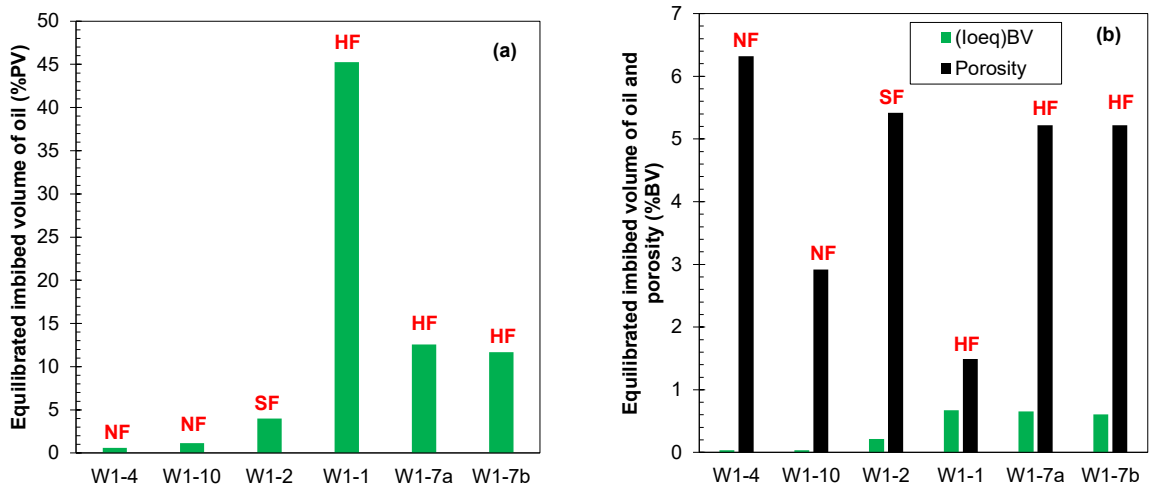

Figure 20 — Equilibrated imbibed oil volume normalized by (a) pore volume (PV) and (b) bulk volume (BV) compared with reported porosity.

$(I_o^{eq})_{BV}$ of plugs shown in **Figure 20b** can be compared with porosity from TRA data listed in **Table 1**. **Figure 20b** shows that $(I_o^{eq})_{BV}$ of HF plugs is fairly closer to their porosity compared with those of SF and NF plugs. $(I_o^{eq})_{BV}$ of SF and NF plugs is much lower than the reported porosity. $(I_o^{eq})_{BV}$ of $W_{1\text{-}1}$ sample is around 0.66% and its porosity is reported as 1.49%. $W_{1\text{-}4}$ and $W_{1\text{-}10}$ plugs have porosity of 6.32% and 2.92%, respectively, but only less than 0.1 % of their BV is imbibed by oil. $W_{1\text{-}7a}$ and $W_{1\text{-}7b}$ plugs have a porosity of 5.22%, and their $(I_o^{eq})_{BV}$ is around 0.6%. $(I_o^{eq})_{BV}$ of these two HF plugs are still low compared to their porosity but are higher than $(I_o^{eq})_{BV}$ of SF and NF plugs. Overall, these observations indicate that pores of the ESB samples are poorly connected. However, the fractures can enhance pore connectivity for liquid imbibition.

Despite the fact that $(I_o^{eq})_{BV}$ of HF plugs is closer to the reported porosity from TRA results (**Table 1**), there is still a significant portion of the pore volume (55 to 88%) that cannot be accessed by the

oil phase. The reported porosity is measured by analyzing crushed rock samples using Boyle's law helium porosimetry. Crushing rock samples creates significant artificial surface area which enhances the accessibility of isolated pores. Hence, ineffective porosity may be converted to effective porosity. The porosity from the TRA report also accounts for artificially-connected pores which were originally isolated, leading to overestimation of effective porosity. Overall, crushing ESB samples with poorly-connected pore network in Boyle's law helium-porosimetry technique gives both the effective and ineffective porosity.

The imbibition profiles in **Figures 6** and **19** are consistent with the evaporation profiles in **Figures 4** and **18**, showing higher Evp_{oil} of HF plugs compared with that of SF followed by NF plugs. Similarly, $(I_o^{eq})_{PV}$ and $(I_o^{eq})_{BV}$ show a similar trend for HF, SF, and NF plugs. These trends can be explained by the role of fractures enhancing the accessibility of isolated pores for oil imbibition and evaporation.

5.2.2 Effect of Fracture on Oil Imbibition

Figure 21 shows the dynamics of oil imbibition into $W_{1\text{-}1}$ plug, highlighting a sequential two-stage process including rapid oil imbibition into fractures followed by slow imbibition from fractures into the rock matrix. This observation is also evident from the imbibition profile of $W_{1\text{-}1}$ plug (**Figure 22a** and **22b**). **Figure 22a**, plotting $(I_o^{eq})_{PV}$ versus time, shows a high-slope region at early times (< 10 hrs) representing fracture filling followed by a low-slope region representing matrix filling.

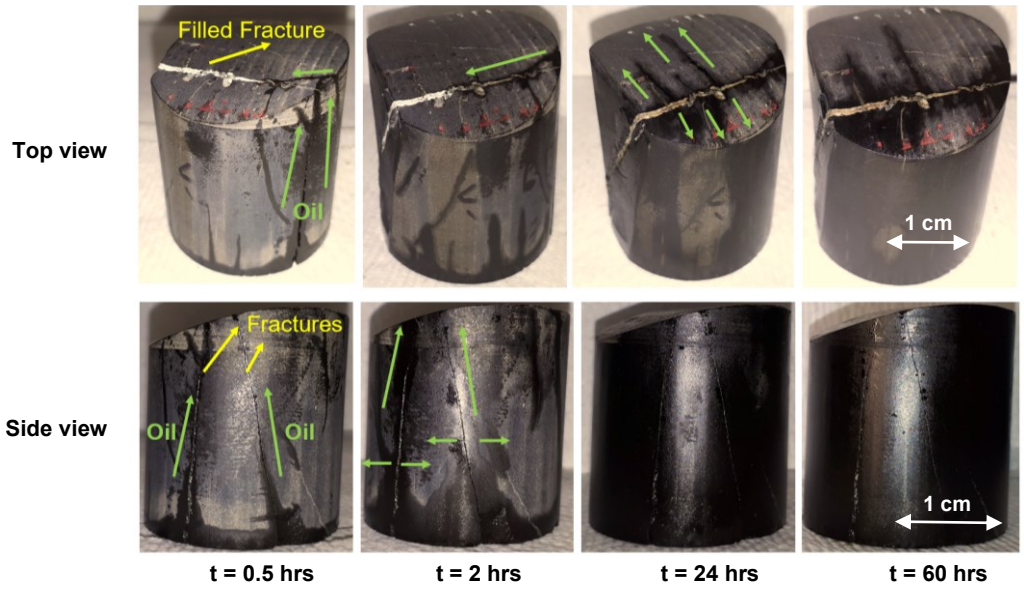

Figure 21 — The pictures of highly-fractured $W_{1\text{-}1}$ plug during oil imbibition process. The first and second rows show the top and side views of the plug. The green arrows show the direction of oil imbibition into the fractures and matrix.

Figure 23a and **23a** compare oil imbibition rate in Stage 1 and Stage 2, respectively, for the SF and HF plugs. Significantly higher Slope 1 compared to Slope 2 is due to high-permeability fractures that rapidly imbibe the oil phase. Slope 1 and Slope 2 of HF plugs are generally higher than those of SF plugs. In **Figure 24**, we compare Slope 1/Slope 2, representing the ratio of imbibition rates in fractures and in rock matrix, for all the plugs. This ratio is 200 for HF $W_{1\text{-}1}$ plug, indicating the significant role of fractures in oil imbibition into this plug. This ratio for HF plugs $W_{1\text{-}7a}$ and $W_{1\text{-}7b}$ is lower than that for SF plugs $W_{1\text{-}6}$ and $W_{1\text{-}9}$. This indicates that although both Slope 1 and Slope 2 are higher for these HF plugs than for SF plugs (**Figure 23a** and **23b**), but the increase in Slope 2 is more significant than in Slope 1 compared with SF plugs.

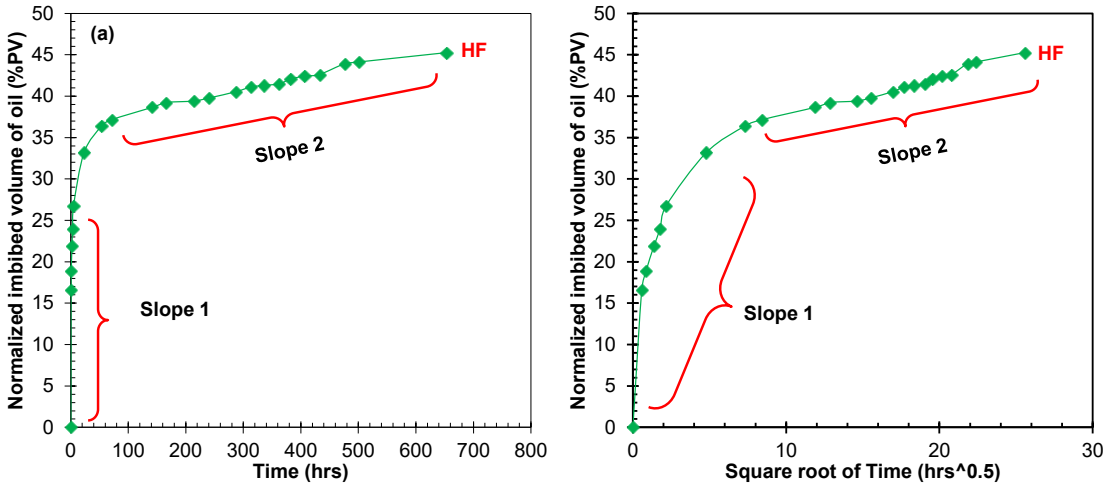

Figure 22 — Normalized volume of oil imbibed into highly-fractured $W_{1\text{-}1}$ plug versus (a) time, and (b) square root of time. The results indicate two different slopes representing fast oil imbibition into fractures and slow imbibition into matrix. The unit of slope is in (a) %PV/hrs; and (b) %PV/hrs^2.

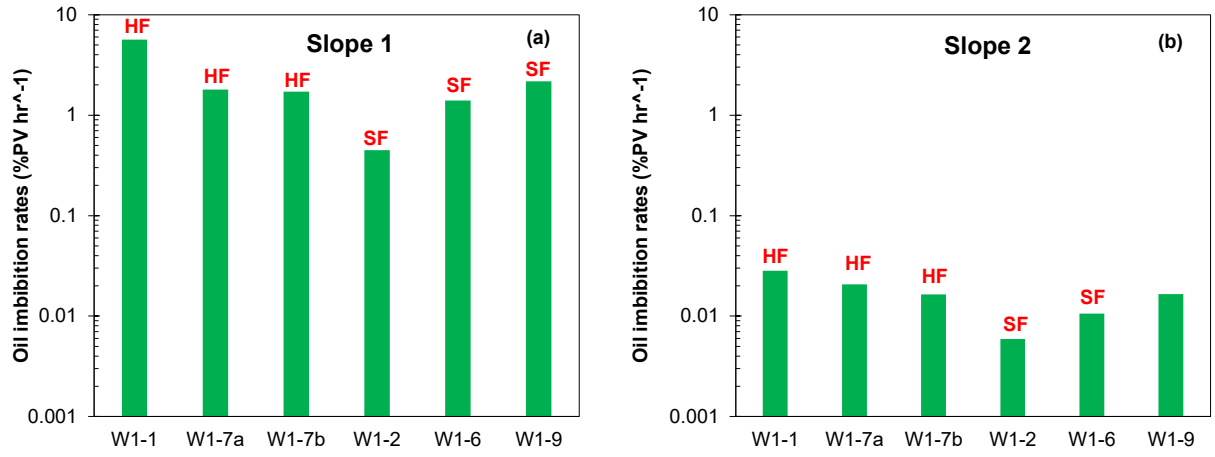

Figure 23 — Comparing oil imbibition rates for the two stages for all HF and SF plugs. (a) Stage 1 represents oil imbibition into fractures and (b) Stage 2 represents oil imbibition into rock matrix.

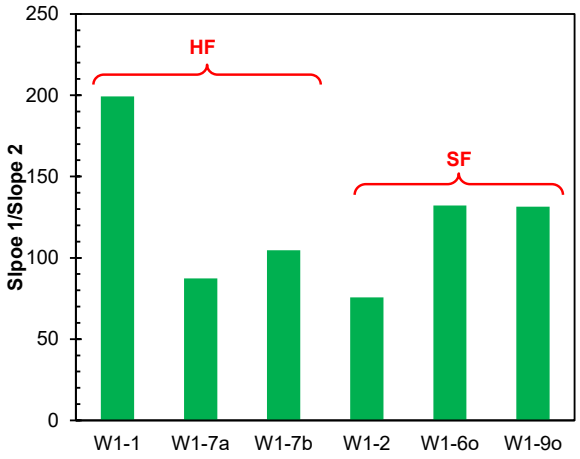

Figure 24 — Slope 1/Slope 2 ratio for all HF and SF plugs.

5.2.3 Effect of Fractures on Oil Recovery

After oil spontaneous imbibition, oil-saturated $W_{1\text{-}1}$ plug is soaked in deionized water in an Amott cell. **Figure 25** shows the picture of oil droplets coming out from the fractures after two months of soaking. Large oil droplets can only be observed along the fractures. Tiny droplets forming on the matrix surface takes much longer time than forming along the fractures. The imbibition oil recovery is mainly attributed to the oil droplets forming along the fractures. This observation is also consistent with the oil imbibition process shown in **Figure 22**. As deionized water imbibes into the fractures, oil is pushed out from the high-permeability fractures faster than being pushed out from the matrix directly.

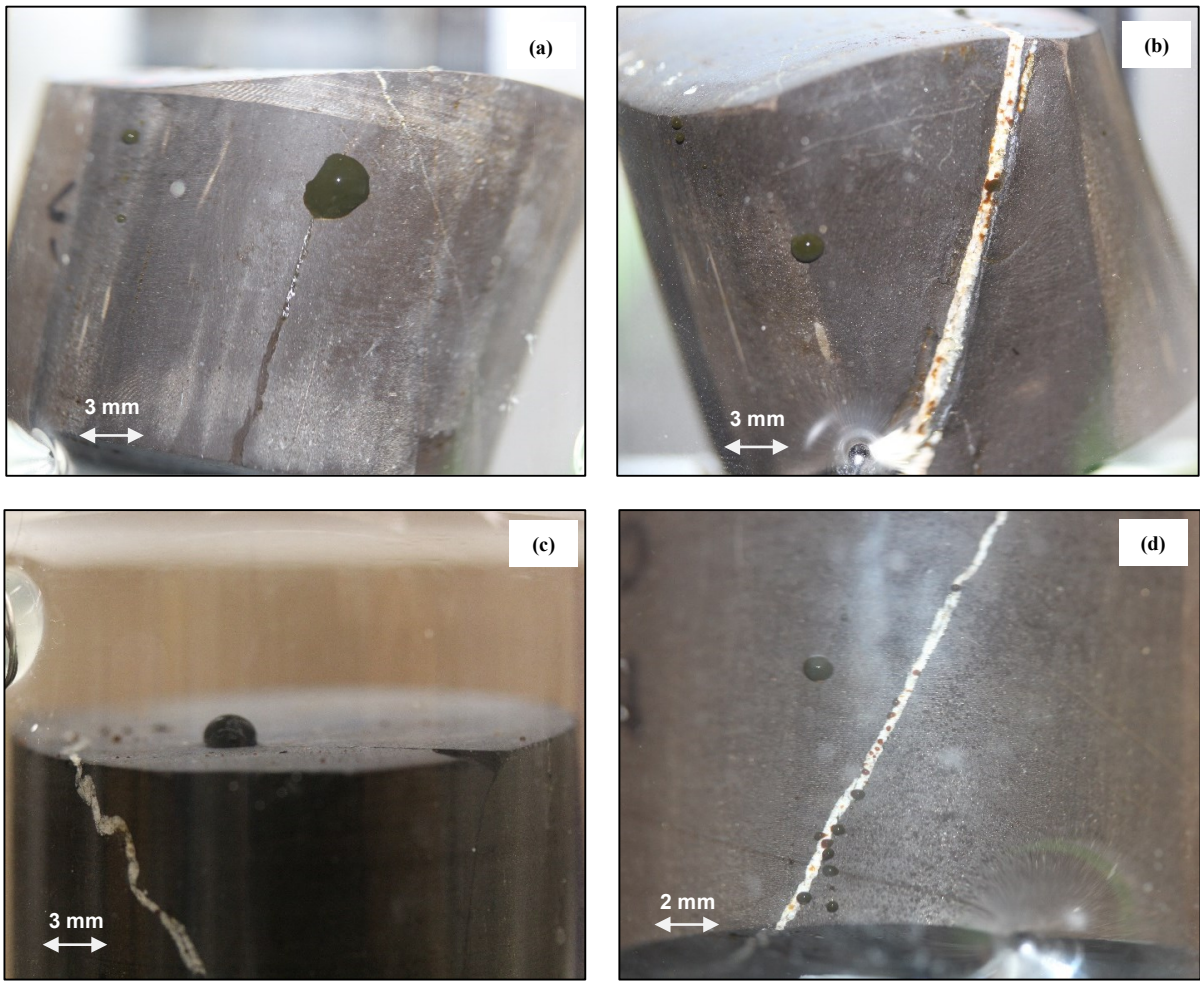

Figure 25 — The pictures of highly-fractured (a)&(b) $W_{1\text{-}1}$ plug after soaking for 2 months and (c)&(d) $W_{1\text{-}7a}$ plug after soaking for 1 month during imbibition-oil recovery process. (a)&(c) show oil droplets forming along the surface of open fracture; (b)&(d) show oil droplets forming along the filled fracture.

Chapter 6

Conclusions and Future Studies

6.1 Conclusions

We investigated wettability of core plugs from East part of the Duvernay Shale Basin (ESB) in the early-oil window and compared the results with those of plugs from the West part of the Shale Basin (WSB) in oil and gas windows. We used CT scan images to characterize the ESB samples in terms of fracture intensity and investigated the effects of fracture intensity on wettability. We discovered the pronounce effects of fractures, thermal maturity, and pore connectivity on evaporation and imbibition profiles.

The results of comparative oil and brine imbibition tests show that the calcite-rich ESB samples have higher wetting affinity to brine than to oil. This observation is opposite to what we previously observed for WSB samples showing a strongly oil-wet behavior. The results of rock-eval pyrolysis show that ESB samples have a higher TOC content and a lower T_{max} (°C) compared with WSB samples. Despite of high TOC content, ESB samples with a low thermal maturity in early-oil window have a less porous organic matter which leads to poorly-connected hydrophobic conduits for oil imbibition. This observation is further confirmed by SEM images of ESB samples, hardly showing pores within the organic matter. The results of oil imbibition tests on samples with different fracture intensity show that highly-fractured plugs imbibe more oil compared with

slightly-fractured plugs, followed by non-fractured plugs.

The key findings of this study are summarized as follows:

Organic-rich shales with low thermal maturity level in early-oil window have limited hydrophobic pores within their organic matter. The observed pores are mainly bordered by inorganic minerals that exhibit hydrophilic characteristics, explaining preferentially water-wet behavior of these shales.

The pore system of shales with high TOC content and low thermal maturity level may not be well connected due to lack of well-developed pores within organic matter.

Pore connectivity of less-mature shales can be enhanced by the existence of fractures that increase the accessibility of isolated pores. Increasing fracture intensity enhances the pore-network connectivity for fluid transport.

Liquid imbibition in fractured rocks follows a two-step process. First, liquid rapidly imbibes into fracture system, and then, it diffuses into the matrix system at a significantly lower rate.

Porosity measurement by using Boyle's law helium-porosimetry on crushed samples overestimates effective porosity of rocks with poorly-connected pores. Crushing shale samples artificially enhances the accessibility of isolated pores which are not part of effective porosity under natural conditions.

Similar to porosity measurement, using crushed shales to measure oil and water saturation of

samples with poorly-connected pores in modified retort technique gives the total fluid content trapped in connected (effective) and isolated (ineffective) pores.

6.2 Implications of the Results

(1) We presented a systematic protocol for qualitative and quantitative analysis of wettability and pore structure of calcareous source rocks by a combined analyses of oil and brine spontaneous imbibition tests, LPGS tests, Scanning Electron Microscopy (SEM) and Energy-dispersive X-ray Spectroscopy (EDS) images.

(2) One may use this finding for selecting sweet spots for shale oil production by evaluating kerogen maturity level of the organic deposits. The discussions and conclusions made for this specific case study of organic-rich calcareous shales can also be applied to evaluate the relationships among wettability, kerogen maturity, pore connectivity, and petrophysical properties of source rocks with similar geological conditions.

(3) The discussions made for brine imbibition into calcareous shales can be applied to selecting salinity of fracturing fluid/drilling fluid used for EOR operations for successful fluid recovery in formations with similar geological conditions.

6.3 Recommendation for Future Studies

Recommendations for future research can be as follows:

(1) In Chapter 3, we discussed the driving forces for brine imbibition by measuring the conductivity of external water. Similar experiments can be conducted on more samples, as well as measuring the ion concentration of the external water before and after brine imbibition to show the salt precipitation/mineral dissolution in a quantitative result.

(2) In chapter 5, we observed different imbibition rates in imbibition profiles in relation to oil imbibing into fracture/matrix. Future studies can be done on simulate the imbibition into fracture/matrix to further investigate into how oil transport in such complex shale matrix.

(3) In chapter 5, we conducted soaking test on fracture plug with deionized water to mainly focus on observing the effect of fracture on oil recovery. In future studies, one can gain knowledge in terms of oil recovery of calcareous shales with different kerogen maturity by conducting counter-current spontaneous imbibition tests with different soaking fluids.

References

Baskin, D. K. (1997). Atomic H/C ratio of kerogen as an estimate of thermal maturity and organic matter conversion. AAPG bulletin, 81(9), 1437-1450. https://doi.org/10.1306/3B05BB14-172A-11D7-8645000102C1865D

Begum, M., Yassin, M. R., & Dehghanpour, H. (2019) Effect of kerogen maturity on organic shale wettability: A Duvernay case study. Marine and Petroleum Geology, 110, 483-496. https://doi.org/10.1016/j.marpetgeo.2019.07.012

Cao, Q., Zhou, W., Deng, H., & Chen, W. (2015). Classification and controlling factors of organic pores in continental shale gas reservoirs based on laboratory experimental results. Journal of Natural Gas Science and Engineering, 27, 1381-1388. https://doi.org/10.1016/j.jngse.2015.10.001

Chenevert, M. E. (1989, January). Lecture: diffusion of water and ions into shales. In ISRM International Symposium. International Society for Rock Mechanics and Rock Engineering.

Chenevert, M. E. (1970). Shale alteration by water adsorption. Journal of petroleum technology, 22(09), 1-141. https://doi.org/10.2118/2401-PA

Chi, L., & Heidari, Z. (2014). Quantifying the impact of natural fractures and pore structure on NMR measurements in multiple-porosity systems. In IPTC 2014: International Petroleum Technology Conference. https://doi.org/10.2523/IPTC-17688-MS

Council, G. W. P. (2009). Modern shale gas development in the United States: A primer.

Department of Energy and National Energy Technology Laboratory, Oklahoma City (2009).

Curtis, J. B. (2002). Fractured shale-gas systems. AAPG bulletin, 86(11), 1921-1938. https://doi.org/10.1306/61EEDDBE-173E-11D7-8645000102C1865D

Dehghanpour, H., Lan, Q., Saeed, Y., Fei, H., & Qi, Z. (2013). Spontaneous imbibition of brine and oil in gas shales: Effect of water adsorption and resulting microfractures. Energy & Fuels, 27(6), 3039-3049. https://doi.org/10.1021/ef4002814

Gale, J. F., & Holder, J. (2010). Natural fractures in some US shales and their importance for gas production. In Geological Society, London, Petroleum Geology Conference Series (Vol. 7, No. 1, pp. 1131-1140). Geological Society of London. https://doi.org/10.1144/0071131

Gao, Z., Fan, Y., Hu, Q., Jiang, Z., Cheng, Y., & Xuan, Q. (2019). A review of shale wettability characterization using spontaneous imbibition experiments. Marine and Petroleum Geology. https://doi.org/10.1016/j.marpetgeo.2019.06.035

Hakim, S. S., Olsson, M. H. M., Sørensen, H. O., Bovet, N., Bohr, J., Feidenhans, R., & Stipp, S. L. S. (2017). Interactions of the calcite {10.4} surface with organic compounds: structure and behaviour at mineral–organic interfaces. Scientific reports, 7(1), 7592. https://doi.org/10.1038/s41598-017-06977-4

Handwerger, D. A., Keller, J., & Vaughn, K. (2011, January). Improved petrophysical core measurements on tight shale reservoirs using retort and crushed samples. In SPE annual technical conference and exhibition. Society of Petroleum Engineers. https://doi.org/10.2118/147456-MS

Handwerger, D. A., Willberg, D. M., Pagels, M., Rowland, B., & Keller, J. F. (2012). Reconciling retort versus dean stark measurements on tight shales. In SPE Annual Technical Conference and Exhibition. Society of Petroleum Engineers. https://doi.org/10.2118/159976-MS

Hu, Y., Devegowda, D., & Sigal, R. (2016). A microscopic characterization of wettability in shale kerogen with varying maturity levels. Journal of Natural Gas Science and Engineering, 33, 1078-1086. https://doi.org/10.1016/j.jngse.2016.06.014

Jagadisan, A., & Heidari, Z. (2019). Experimental quantification of the effect of thermal maturity of kerogen on its wettability. SPE Reservoir Evaluation & Engineering, 22(04), 1-323. https://doi.org/10.2118/195684-PA

Kesserwan, H., Jin, G., Agrawal, G., & Sultan, A. (2016). Wettability characterization and comparison of carbonate source rocks using NMR. Society of Petrophysicists and Well-Log Analysts.

Lan, Q., Xu, M., Binazadeh, M., Dehghanpour, H., & Wood, J. M. (2015). A comparative investigation of shale wettability: The significance of pore connectivity. Journal of Natural Gas Science and Engineering, 27, 1174-1188. https://doi.org/10.1016/j.jngse.2015.09.064

Landry*, C. J., Tokan-Lawal, A., Eichhubl, P., & Prodanovic, M. (2014). Matrix-fracture connectivity in eagle ford shale. In Unconventional Resources Technology Conference, Denver, Colorado, 25-27 August 2014 (pp. 619-628). Society of Exploration Geophysicists, American Association of Petroleum Geologists, Society of Petroleum Engineers.

https://doi.org/10.15530/urtec-2014-1922708

Law, C. A. (1999). Evaluating source rocks. AAPG Special Volumes. Treatise of Petroleum Geology/Handbook of Petroleum Geology, 3, 6-1.

Liang, F., Lai, B., Zhang, J., Liu, H.-H., & Li, W. (2018). An experimental study on interactions between imbibed fracturing fluid and organic-rich tight carbonate source rocks. Society of Petroleum Engineers. https://doi.org/10.2118/188338-PA

Loucks, R. G., Reed, R. M., Ruppel, S. C., & Hammes, U. (2010). Preliminary classification of matrix pores in mudrocks: Gulf Coast Association of Geological Societies Transactions, v. 60, p. 435-441.

Luo, P., & Zhong, N. (2020). The role of residual bitumen on the pore structure of organic-rich shales from low to over mature: Insight from shale and coal samples after the hydrous pyrolysis. International Journal of Coal Geology, 103515. https://doi.org/10.1016/j.coal.2020.103515

Marshall, F.H., Corlett, H., Lyster, S. and Berhane, H. (2019): Three-dimensional property model of the Duvernay Formation in Alberta (dataset, multiple files); Alberta Energy Regulator / Alberta Geological Survey, AER/AGS Model 2019-02.

Munson, E. O. (2015). Reservoir characterization of the Duvernay Formation, Alberta: A pore-to basin-scale investigation (Doctoral dissertation, University of British Columbia). http://dx.doi.org/10.14288/1.0166722

Odusina, E. O., Sondergeld, C. H., & Rai, C. S. (2011). NMR Study of Shale Wettability. Society of Petroleum Engineers. https://doi.org/10.2118/147371-MS

Prodanovic, M., Bryant, S. L., & Karpyn, Z. T. (2010). Investigating matrix/fracture transfer via a level set method for drainage and imbibition. SPE Journal, 15(01), 125-136. https://doi.org/10.2118/116110-PA

Requejo, A. G., Gray, N. R., Freund, H., Thomann, H., Melchior, M.T., L.A. Gebhard, M. Bernardo, C.F. Pictroski, & C.S. Hsu (1992). Maturation of petroleum source rocks. 1. Changes in kerogen structure and composition associated with hydrocarbon generation. Energy & fuels, 6(2), 203-214. https://doi.org/10.1021/ef00032a015

Roychaudhuri, B., Tsotsis, T. T., & Jessen, K. (2013). An experimental investigation of spontaneous imbibition in gas shales. Journal of Petroleum Science and Engineering, 111, 87-97 https://doi.org/10.1016/j.petrol.2013.10.002

Schrader, M. E., & Yariv, S. (1990). Wettability of clay minerals. Journal of colloid and interface science, 136(1), 85-94. https://doi.org/10.1016/0021-9797(90)90080-8

Sigal, R. F. (2015). Pore-size distributions for organic-shale-reservoir rocks from nuclear-magnetic-resonance spectra combined with adsorption measurements. SPE Journal, 20(04), 824-830. https://doi.org/10.2118/174546-PA

Stoakes, F. A. (1980). Nature and control of shale basin fill and its effect on reef growth and termination: Upper Devonian Duvernay and Ireton formations of Alberta, Canada. Bulletin of

Canadian Petroleum Geology, 28(3), 345-410.

Sulucarnain, I.D., Sondergeld, C.H., & Rai, C.S. (2012). An NMR study of shale wettability and effective surface relaxivity. In SPE Canadian Unconventional Resources Conference. Society of Petroleum Engineers. https://doi.org/10.2118/162236-MS

Switzer, S. B., Holland, W. G., Christie, D. S., Graf, G. C., Hedinger, A. S., McAuley, R. J., Wierzbicki, R.A., Packard, J.J., Mossop, G.D., & Shetsen, I. (1994). Devonian Woodbend-Winterburn strata of the Western Canada sedimentary basin. Geological Atlas of the Western Canada Sedimentary Basin: Canadian Society of Petroleum Geologists and Alberta Research Council, 165-202.

Takahashi, S., & Kovscek, A. R. (2010). Spontaneous countercurrent imbibition and forced displacement characteristics of low-permeability, siliceous shale rocks. Journal of Petroleum Science and Engineering, 71(1-2), 47-55. https://doi.org/10.1016/j.petrol.2010.01.003

Takahashi, S., & Kovscek, A. R. (2010). Wettability estimation of low-permeability, siliceous shale using surface forces. Journal of Petroleum Science and Engineering, 75(1-2), 33-43 https://doi.org/10.1016/j.petrol.2010.10.008

Taylor, R. K., & Smith, T. J. (1986). The engineering geology of clay minerals: swelling, shrinking and mudrock breakdown. Clay Minerals, 21(3), 235-260. https://doi.org/10.1180/claymin.1986.021.3.01

Van Krevelen, D. W. (1950). Graphical-statistical method for the study of structure and reaction

processes of coal. Fuel, 29, 269-284.

Vega, B., Ross, C. M., & Kovscek, A. (2014). Imaging-based characterization of calcite-filled fractures and porosity in shales. In Unconventional Resources Technology Conference, Denver, Colorado, 25-27 August 2014 (pp. 988-1005). Society of Exploration Geophysicists, American Association of Petroleum Geologists, Society of Petroleum Engineers. https://doi.org/10.15530/urtec-2014-1922521

Walter, S., Beavis, K., Whibbs, C., Stricker, S., Preston, A., Jenkins, J., & Hein, F. (2016). Recognizing Duvernay B-carbonate distribution and its potential implications on resource and reserve estimations. In AAPG Annual Convention and Exibition, Calgary, Alberta.

Wang, P., Chen, Z., Pang, X., Hu, K., Sun, M., & Chen, X. (2016). Revised models for determining TOC in shale play: Example from Devonian Duvernay shale, Western Canada sedimentary basin. Marine and Petroleum Geology, 70, 304-319. https://doi.org/10.1016/j.marpetgeo.2015.11.023

Wendte, J., Dravis, J. J., Stasiuk, L. D., Qing, H., Moore, S. L., & Ward, G. (1998). High-temperature saline (thermoflux) dolomitization of Devonian Swan Hills platform and bank carbonates, Wild River area, west-central Alberta. Bulletin of Canadian Petroleum Geology, 46(2), 210-265.

Xu, M., & Dehghanpour, H. (2014). Advances in understanding wettability of gas shales. Energy & Fuels, 28(7), 4362-4375. https://doi.org/10.1021/ef500428y

Xu, S., Yassin, M. R., Dehghanpour, H., & Kolbeck, C. (2020, September). Wettability of Calcareous Shales from the East Duvernay Basin: The Role of Natural Fractures, Thermal Maturity, and Organic-Pore Connectivity. In SPE Canada Unconventional Resources Conference. OnePetro. https://doi.org/10.2118/199971-MS

Yang, R., Hu, Q., Yi, J., Zhang, B., He, S., Guo, X., Hou, Y. and Dong, T., 2019. The effects of mineral composition, TOC content and pore structure on spontaneous imbibition in Lower Jurassic Dongyuemiao shale reservoirs. Marine and Petroleum Geology, 109, pp.268-278. https://doi.org/10.1016/j.marpetgeo.2019.06.003

Yassin, M. R., Begum, M., & Dehghanpour, H. (2017). Organic shale wettability and its relationship to other petrophysical properties: A Duvernay case study. International Journal of Coal Geology, 169, 74-91. https://doi.org/10.1016/j.coal.2016.11.015

Zhang, S., Li, Y., & Pu, H. (2020). Studies of the storage and transport of water and oil in organic-rich shale using vacuum imbibition method. Fuel, 266, 117096. https://doi.org/10.1016/j.fuel.2020.117096

Zolfaghari, A., Dehghanpour, H., & Xu, M. (2017). Water sorption behaviour of gas shales: II. Pore size distribution. International Journal of Coal Geology, 179, 187-195, https://doi.org/10.1016/j.coal.2017.05.009.

Zygler, A., Słomińska, M., & Namieśnik, J. (2012). 2.04-Soxhlet Extraction and New Developments Such as Soxtec. Comprehensive Sampling and Sample Preparation, 65-82.

https://doi.org/10.1016/B978-0-12-381373-2.00037-5

Appendix A

Well Log Data, Tight-Rock Analysis (TRA), X-Ray Diffraction (XRD), Rock-Eval Pyrolysis, and CT Scan Methodology

Well log data. **Figure 26** presents log data of Well 1 as an example showing how we select our samples from the identified Upper Duvernay, Carbonate, Middle Duvernay, and Lower Duvernay layers. The Upper Duvernay is a source rock with high TOC content as indicated by the high gamma ray (GR) and resistivity. It contains interbedded source rocks of various quality, with minor interbeds of non-source rocks. The Carbonate layer with low porosity is not considered to be a source rock or a reservoir rock. This layer with about ten meters thickness has very low TOC content and can be considered as a barrier for the induced hydraulic fractures. Below the Carbonate layer are the Middle and Lower Duvernay layers which are referred to as "Lower Duvernay" as a single layer (Munson, 2015; Walter et al., 2016). Similar to Upper Duvernay, these two layers are excellent source rocks which have interbeds with high TOC content (up to 11.78 wt% as listed in **Table 3**). We selected samples from the upper, middle, and lower Duvernay layers which have interbeds with high TOC content based on the log data.

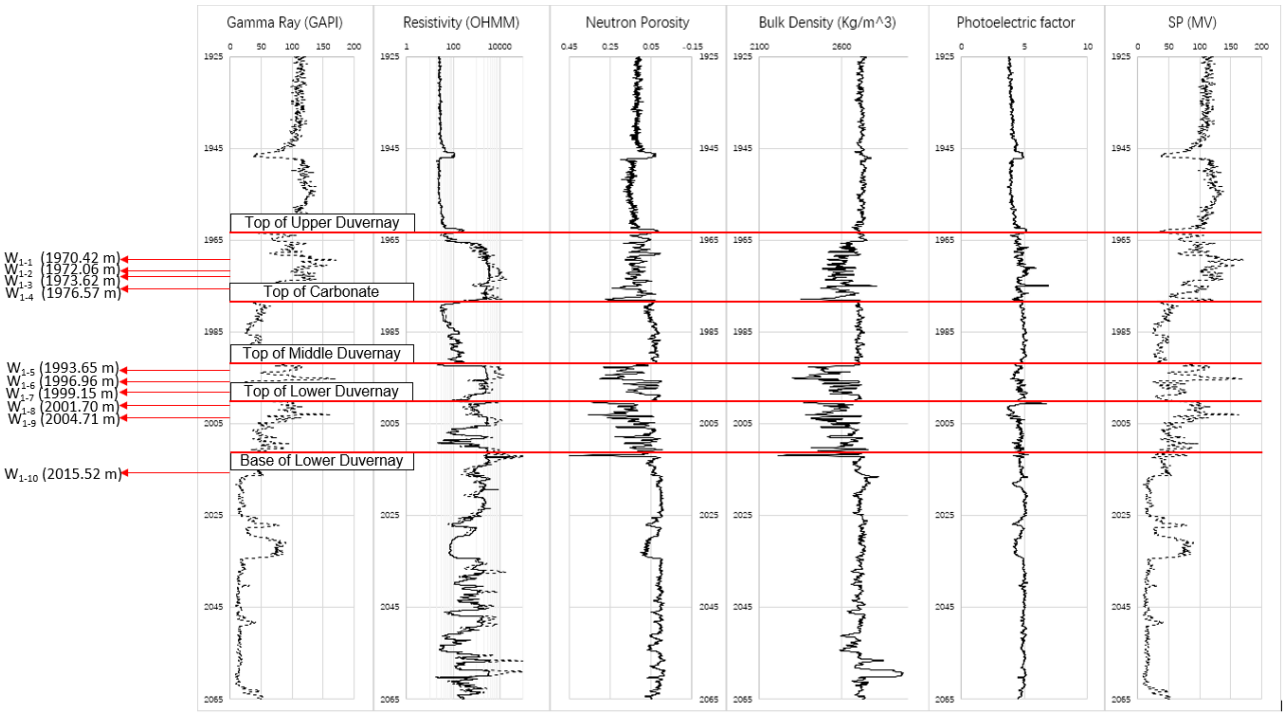

Figure 26 — Well log data of the cored well (Well 1) showing selection of core plugs from upper, middle, and lower Duvernay layers.

Tight-Rock Analysis. A commercial laboratory measured as-received bulk density on off-set samples with initial fluids in place. Then they crushed the as-received samples and measured matrix density and gas-filled porosity on crushed samples by using Boyle's law helium-porosimetry. Modified-retort technique was then used to extract pore fluids to calculate effective porosity and fluid saturations. The crushed samples were heated continuously at three characteristic retort temperatures. At each temperature, pore fluids were vaporized and extracted from the samples (Handwerger et al., 2012). The extracted vapors were condensed and measured to give initial oil and water saturations. Effective porosity was calculated as gas-filled porosity plus extracted oil and water contents (Handwerger et al., 2011). The permeability was measured

using pressure-decay method on off-set crushed samples with initial fluids in place. More details regarding the experimental procedure can be found elsewhere (Handwerger et al., 2011; Handwerger et al., 2012).

Minerology. A commercial laboratory conducted semi-quantitative x-ray diffraction (XRD) analysis on five off-set samples to characterize the overall minerology, and in particular, the type and concentration of clay minerals. The percentage of expandable clays was determined based on the amount of interlayered smectite (swelling clay) in the illite/smectite mixed layers (Taylor and Smith, 1986).

Rock-Eval Pyrolysis. A commercial laboratory conducted rock-eval pyrolysis tests on ten off-set samples to determine total TOC content (wt%), kerogen type, and kerogen maturity. The results include the amount of TOC and the values of S_1, S_2, S_3, Hydrogen Index (HI), Oxygen Index (OI), and Production Index (PI). The TOC content represents the organic carbon of the samples (Baskin, 1997). S_1 is the amount of free hydrocarbons in the samples in milligrams of hydrocarbon per gram of rock. S_2 is the amount of hydrocarbons generated through thermal cracking of non-volatile organic matter (OM). S_2 indicates the hydrocarbon production potential of the rock if burial and maturation continue. S_3 is the amount of CO_2 produced during pyrolysis of kerogen. T_{max} is the temperature when the release of hydrocarbons from cracking of non-volatile organic matter reaches the maximum amount during pyrolysis. It indicates the maturation stage of the organic matter (Baskin, 1997). HI is calculated using TOC content and S_2, and is used to characterize the type of organic matter. OI is calculated using TOC content and S_3, and represents the amount of oxygen relative to the amount of organic carbon (Law, 1999). PI is the production index which is

used to characterize the maturity level of the organic matter. PI is calculated based on the values of S_1 and S_2 (Law, 1999).

CT Scan. Computerized tomography (CT) scan of the core plugs was conducted by a commercial laboratory to detect intensity of fractures. Depending on the degree of fracture intensity, the core plugs were categorized into highly-fractured (HF), slightly-fractured (SF), and non-fractured (NF) plugs.

Appendix B

Sample Heating and Toluene Extraction

To investigate if any residual oil can be released from core plugs after sample heating, we cleaned $W_{1\text{-}8}$ core plug using Soxhlet extraction method. Core plug $W_{1\text{-}8}$ was coated with filter paper and placed in the extraction thimble of a Soxhlet extractor. Toluene was used as the extraction solvent and vapors of toluene produced in a distillation flask passed through the thimble and liquified in a condenser. Extracted oil was carried with condensed toluene and fell back to the distillation flask. Then, fresh toluene vapors from the distillation flask passed back into the thimble to further extract residual oil. The process was repeated for a duration of 14 days. More details of Soxhlet extraction method can be found elsewhere (Zygler et al., 2012). Then, core plug $W_{1\text{-}8}$ was heated at 90ºC to reach the equilibrated mass.

Figure 27 shows oil evaporation profile of $W_{1\text{-}8}$ core plug before toluene extraction. After being treated with toluene using Soxhlet extraction method and heated to reach the equilibrated state, the

equilibrated mass is compared with the heated mass of as-received plug as shown in **Figure 28**. We observed that there is a tiny difference between the two values (85.386 g vs. 85.342 g). This result suggests that heating process can evaporate most of the oil in the connected pore space. Oil that cannot be evaporated by heating may be trapped in isolated pores which cannot be accessed by extraction solvents such as toluene.

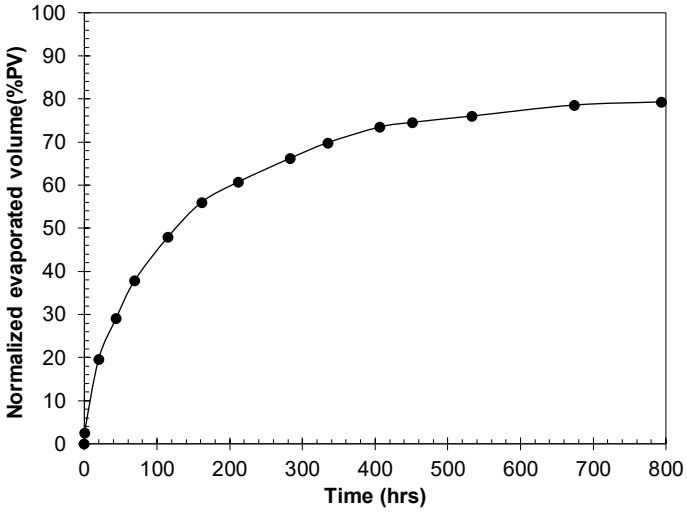

Figure 27 — Normalized evaporated oil volume (Evp_{oil}) vs. time of core plug $W_{1\text{-}8}$ prepared for toluene extraction.

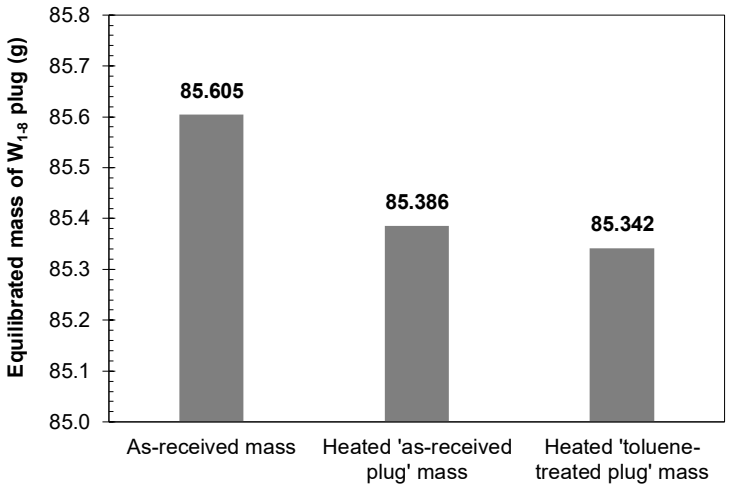

Figure 28 — Comparison of equilibrated mass of $W_{1\text{-}8}$ plug at different conditions.

Appendix C

Calculation of $(I_o^{eq})_{PV}$, $(I_w^{eq})_{PV}$, and WI_o

The equilibrated imbibed volumes of oil and brine were normalized by BV ($(I_o^{eq})_{BV}$ and $(I_w^{eq})_{BV}$) and by PV ($(I_o^{eq})_{PV}$ and $(I_w^{eq})_{PV}$):

$$(I_o{}^{eq})_{BV} = \frac{\text{Equilibrated imbibed volume of oil}}{\text{Bulk volume}} \times 100$$

$$(I_w{}^{eq})_{BV} = \frac{\text{Equilibrated imbibed volume of brine}}{\text{Bulk volume}} \times 100$$

$$(I_o{}^{eq})_{PV} = \frac{\text{Equilibrated imbibed volume of oil}}{\text{Pore volume}} \times 100$$

$$(I_w{}^{eq})_{PV} = \frac{\text{Equilibrated imbibed volume of brine}}{\text{Pore volume}} \times 100$$

Oil wettability index (WI_o) is defined as:

$$WI_o = \frac{(I_o{}^{eq})_{PV}}{(I_o{}^{eq})_{PV} + (I_w{}^{eq})_{PV}}$$

Appendix D

Brine Analysis Results

Table 8 lists the ion concentration of the early-flowback brine sample used in imbibition tests.

Table 8 — Ion concentration of early-flowback brine sample.

Ions	Na^+	Mg^{2+}	K^+	Ca^{2+}	Cl^-	HCO_3^-	SO_4^{2-}	CO_3^{2-}	OH^-	TDS
Concentration (ppm)	59,701	1,682	2,663	11,682	121,734	232	746	0	0	198,440